

1 A global wave parameter database for geophysical  
2 applications. Part 3: improved forcing and spectral  
3 resolution

4 Matias Alday<sup>a</sup>, Mickael Accensi<sup>a</sup>, Fabrice Ardhuin<sup>a,b</sup>

5 <sup>a</sup>*Univ. Brest, CNRS, Ifremer, IRD, Laboratoire d'Océanographie Physique et Spatiale,*  
6 *Brest, France*

7 <sup>b</sup>*Scripps Institution of Oceanography, University of California San Diego, La Jolla,*  
8 *California*

---

9 **Abstract**

Numerical wave models are used for a wide range of applications, from the global ocean to coastal scales. Here we report on significant improvements compared to the previous hindcast by Rascle and Ardhuin (2013). This result was obtained by updating forcing fields, adjusting the spectral discretization and retuning wind wave growth and swell dissipation parameters. Most of the performance analysis is done using significant wave heights ( $H_s$ ) from the recent re-calibrated and denoised satellite altimeter data set provided by the European Space Agency Climate Change Initiative (ESA-CCI), with additional verification using spectral buoy data. We find that, for the year 2011, using wind fields from the recent ERA5 reanalysis provides lower scatter against satellite  $H_s$  data compared to historical ECMWF operational analyses, but still yields a low bias on wave heights that can be mitigated by re-scaling wind speeds larger than 20 m/s. Alternative blended wind products can provide more accurate forcing in some regions, but were not retained because of larger errors elsewhere. We use the shape of the probability density function of  $H_s$  around 2 m to fine tune the swell dissipation parameterization. The updated model hindcast appears to be generally more accurate than the previous version, and can be more accurate than the ERA5  $H_s$  estimates, in particular in strong current regions and for  $H_s > 7$  m.

10 *Keywords:* Wind-generated waves, WAVEWATCH III

## 11 1. Introduction

12 Spectral wave models are routinely used for many applications in Earth  
13 sciences and ocean engineering. Global and regional wave data-sets gener-  
14 ated through models such as WAM (WAMDI Group, 1988; Bidlot, 2005) or  
15 WAVEWATCH III<sup>®</sup>(The WAVEWATCH III <sup>®</sup> Development Group, 2019)  
16 have helped to increase our understanding of the wind-generated waves' dy-  
17 namics, estimate ocean-atmosphere interactions (e.g. surface drift and air-  
18 sea fluxes), analyze extreme events occurrences, define operational conditions  
19 for shipping, offshore and port activities, and assess wave energy resources,  
20 just to name a few examples. New applications, for example in seismology  
21 (e.g. Lecocq et al., 2019) are made possible by the ever increasing quality of  
22 modeled wave spectra and other associated parameters.

23 The hindcast presented by Rasclé et al. (2013) has been used in a wide  
24 range of applications, including as a source of boundary conditions for coastal  
25 models (Roland and Ardhuin, 2014; Boudière et al., 2013). For most open  
26 ocean regions, the accuracy of significant wave height ( $H_s$ ) estimates is typ-  
27 ically better than 10%, with great benefits for the safety of life at sea, but  
28 some regions, in enclosed seas, regions of strong currents, and near the sea  
29 ice,  $H_s$  errors typically exceed 20%, and other parameters can be much less  
30 accurate, in particular the shape of the frequency spectrum, the height of  
31 swells or the directional spreading (Stopa et al., 2016b). The reasons for  
32 these errors, and some first steps to reduce them, are the main topic of the  
33 present paper. In general the quality of numerical wave model output is a  
34 function of at least three factors, in decreasing order of importance. First,  
35 the accuracy of forcing fields (e.g. Cavaleri and Bertotti, 1997), second, the  
36 realism of parameterization of processes representing spectral wave evolu-  
37 tion (e.g. Ardhuin et al., 2010) and third, the numerical choices made to  
38 integrate the Wave Action Equation, namely discretization and numerical  
39 schemes (e.g. Tolman, 1995; Roland and Ardhuin, 2014).

40 The present paper presents the effect of adjustment to model parameter-  
41 ization in section 2, the impact of forcing field choices in section 3, and the  
42 influence of model discretization in section 4. We briefly discuss in section 5  
43 alternative parameterizations that can lead to clear improvements for some  
44 parameters most sensitive to the higher frequencies of the sea state but that,  
45 so far, have not led to improvements in  $H_s$  estimates and will probably re-  
46 quire further adjustments and have thus not yet been used for the hindcast  
47 presented here. The global validation presented in section 6 show a clear im-

48 improvement on sea state parameters produced by Rascle and Ardhuin (2013)  
49 and, for specific conditions, also an improvement on the  $H_s$  estimates in the  
50 ERA5 reanalysis. Conclusions follow in section 6.

## 51 **2. Model setup**

### 52 *2.1. Forcing fields*

53 Because waves are forced by the wind, are damped by sea ice, and are  
54 strongly modified by currents, any improvement in the knowledge of these  
55 three forcing fields should result in better wave model results.

56 One of the main features in the generation of the wave hindcast analyzed  
57 in the present study, is the utilization of the wind fields from the fifth genera-  
58 tion ECMWF atmospheric reanalyses of the global atmosphere, ERA5 (Hers-  
59 bach et al., 2020), and the introduction of satellite-derived merged surface  
60 current product that combines geostrophic and Ekman currents, as produced  
61 by the Copernicus Marine Environment Monitoring System (CMEMS). The  
62 ERA5 reanalysis was developed using 4D-Var data assimilation from the Inte-  
63 grated Forecast System (IFS) model cycle 41r2. The number of observations  
64 assimilated from different measurement sources goes from 0.75 million per  
65 day in 1979 to approx. 24 million in 2018. The hourly output wind fields  
66 with a 31 km horizontal grid resolution, represents a clear increase in detail  
67 compared with some of its predecessors, like ERA-Interim (Dee et al., 2011).  
68 Still, the limited horizontal resolution makes the ERA5 wind fields less well  
69 resolved than those of recent ECMWF operational analyses that use a T799  
70 Gaussian grid with an equivalent resolution of 25 km. Rivas and Stoffelen  
71 (2019) showed that ERA5 winds have a root mean square difference with the  
72 ASCAT winds that is 20% lower compared to ERA-Interim. Still, at wind  
73 speeds above 20 m/s, ERA5 biases may be as large as -5 m/s (Pineau-Guillou  
74 et al., 2018), which should have a very important impact on waves modeled  
75 with ERA5 winds.

76 The surface current fields were taken from the CMEMS-Globcurrent prod-  
77 uct (Global Ocean Multi Observation Product, MULTIOBS\_GLO\_PHY\_RE-  
78 P\_015\_004), with a resolution of 3 hour in time, and 0.25 degrees in latitude  
79 and longitude. This current field is the sum of geostrophic and Ekman com-  
80 ponents based on the method of Rio et al. (2014), using a new mean dynamic  
81 topography (Rio M-H, S. Mulet, H. Etienne, G. Dibarboure, N. Picot. The  
82 new CNES-CLS18 Global Mean Dynamic Topography).

83 Finally, the ice concentration is taken from the Ifremer SSMI-derived daily  
 84 product (Girard-Ardhuin and Ezraty, 2012). For ice thickness, that matters  
 85 most near the ice edge where it is poorly known, we have used a constant  
 86 1 m ice thickness. Partial blocking of waves by icebergs is represented fol-  
 87 lowing Ardhuin et al. (2011) using the Ifremer-Altiberg icebergs distribution  
 88 database Tournadre et al. (2015).

## 89 2.2. Adjusted parametrizations and parameters

90 Atmosphere-wave interactions include both wave generation as parame-  
 91 terized by Janssen (1991) with modifications by Bidlot et al. (2005, 2007) and  
 92 swell damping, and the air-sea friction effect of Ardhuin et al. (2009). The  
 93 details and adjustments of these parameterizations are described in Ardhuin  
 94 et al. (2010), and Leckler (2013). Here we only recall equations in which  
 95 appear the parameters that we have tuned in the present work. A more  
 96 comprehensive description can be found in The WAVEWATCH III<sup>®</sup> Devel-  
 97 opment Group (2019).

98 In particular, the wind input source term was reduced by using a modified  
 99 friction velocity  $u_*$  with a frequency dependent term  $u'_*$ , similar to what was  
 100 done by Chen and Belcher (2000). Eqs. (20) in Ardhuin et al. (2010) is

$$S_{\text{atm}}(f, \theta) = S_{\text{out}}(f, \theta) + \frac{\rho_a}{\rho_w} \frac{\beta_{\text{max}}}{\kappa^2 \exp(Z) Z^4 \left(\frac{u_*}{C}\right)^2} \quad (1)$$

$$\times \max\{\cos(\theta - \theta_u), 0\}^p \sigma F(f, \theta) \quad (2)$$

101 where  $Z = \log(\mu)$ , with  $\mu$  the dimensionless critical height as given by Janssen  
 102 (1991, eq. 16).

103 In eq. (1)  $\beta_{\text{max}}$  is a non-dimensional wind-wave growth coefficient that  
 104 has been used as a tuning parameter to calibrate for wind strength biases  
 105 (e.g. Stopa et al., 2019). We will revisit this tuning for ERA5 winds in the  
 106 present paper.

107 The swell dissipation parameterization is based on observations of ocean  
 108 swell evolution from satellite data (Ardhuin et al., 2009). It includes expres-  
 109 sions to take into account the effects of the transitions from (linear) viscous  
 110 boundary layer to (non-linear) turbulent boundary layer. The smoothing  
 111 between these two regimes accounts for the Rayleigh distribution of wave  
 112 heights (Perignon et al., 2014). The negative part of the wave-atmosphere  
 113 interaction, is thus parameterized as follows,

$$S_{\text{out}}(k, \theta) = r_{\text{vis}} S_{\text{out,vis}}(k, \theta) + r_{\text{tur}} S_{\text{out,tur}}(k, \theta), \quad (3)$$

114 where the two weights give the relative importance of viscous and turbulent  
 115 attenuation, and are controlled by the ratio of the significant Reynolds number  
 116  $\text{Re} = 2u_{\text{orb},s}H_s/\nu_a$  and its critical value  $\text{Re}_c$ .

$$r_{\text{vis}} = 0.5 [1 - \tanh((\text{Re} - \text{Re}_c)/s_7)] \quad (4)$$

$$r_{\text{tur}} = 0.5 [1 + \tanh((\text{Re} - \text{Re}_c)/s_7)]. \quad (5)$$

117 Based on the analogy with oscillatory bottom boundary layers,  $\text{Re}_c$  was ini-  
 118 tially set to  $1.5 \times 10^5$ .

119 Wave energy loss to the ocean is dominated by wave breaking, and param-  
 120 eterized following the saturation-based breaking ideas of Phillips (1985). An  
 121 ad hoc "cumulative term" was added to enhance the dissipation of relatively  
 122 short waves (Banner and Morison, 2006; Ardhuin et al., 2010). Alternatives  
 123 are discussed in section 5.

124 Finally, for economical reasons, we have used the Discrete Interaction  
 125 Approximation (DIA Hasselmann and Hasselmann, 1985), to represent the  
 126 4-wave nonlinear interactions. This rather crude parameterization induces  
 127 errors that are partly corrected by the other adjusted source terms in the  
 128 Wave Action Equation (Young and van Vledder, 1993).

### 129 *2.3. Spectral and spatial discretization*

130 The wave spectrum (spectral grid) is discretized in 24 directions, equiva-  
 131 lent to a  $15^\circ$  directional resolution, and 36 exponentially spaced frequencies  
 132 from 0.0339 to 0.95267 Hz, with a 1.1 increment factor from one frequency to  
 133 the next. The selected frequency range represents a departure from previous  
 134 studies (like Stopa et al. (2016a) and Rascle and Ardhuin (2013), in which  
 135 a narrower frequency range was employed, from 0.037 to 0.71 Hz. Although  
 136 the parameterizations used here are not very accurate for frequencies above  
 137 3 times the wind sea peak (e.g. Peureux et al., 2018), the extension to higher  
 138 frequencies allows to better capture the variability of the wave spectrum for  
 139 very low wind speeds or very short fetches. The lower frequencies are there  
 140 to let the spectrum develop for the most severe storm cases (Hanafin et al.,  
 141 2012). We note that we have used the third order Upwind Quickest advec-  
 142 tion schemes (Leonard, 1991) for both spatial and spectral advection, and  
 143 the correction for the Garden Sprinkler Effect proposed by Tolman (2002).

144 All the model testing and tuning presented in section 2 was performed  
 145 over a near-global grid with a spatial resolution of  $0.5^\circ$ , from  $78^\circ$  S to  $83^\circ$  N

146 in latitude. However, all the other results, including the final hindcast, use  
 147 a multi-grid system (Tolman, 2008; Chawla et al., 2013) in which regional  
 148 grids provide a refinement near the coasts, the ice edge, and in regions of  
 149 strong currents. A total of 7 nested grids were placed within the global grid,  
 150 6 regular grids and 1 curvilinear grid for the Arctic region. Details of the  
 151 nested grids are provided in table 1 and Fig. 1. As shown in Fig. 1, only  
 152 sections of the complete domains are used to perform calculations within  
 153 each grid, those sections with active grid nodes are highlighted with different  
 154 colors. The boundary conditions from a higher rank grid are taken at the  
 155 edges of the colored regions in Fig. 1 from the lower rank grid, and the higher  
 156 rank grid results are spatially averaged to give the lower rank grid solution  
 157 where these overlap (Tolman, 2008).

Sub-Grid Name	Region	Grid type	Spatial resolution	Rank
ATNE-10M	North-East Atlantic	regular	1/6°	2
ATNW-10M	North-West Pacific	regular	1/6°	3
Africa-10M	Africa	regular	1/60°	3
PACE-10M	North-East Pacific	regular	1/6°	2
CRB-3M	Caribbean Sea	regular	1/20°	3
NC-3M	New Caledonia and Vanuatu	regular	1/20°	3
ARC-12K	Arctic Ocean	curvilinear	12 km	4

Table 1: Nested grids characteristics. Global grid is defined as rank 1.

158 The benefits of the multi-grid system are particularly discussed in section  
 159 4.1. Including the Arctic grid allowed to provide a truly global wave hindcast.

#### 160 2.4. Model tuning

161 The value of  $\beta_{\max}$  in eq. (1),  $s_7$  and  $\text{Re}_c$  in eqs. (4) and (5) have been  
 162 adjusted to minimize the model differences against satellite altimeter mea-  
 163 surements of  $H_s$  by the Jason-2 mission for the year 2011, using the European  
 164 Space Agency Climate Change Initiative data set (Dodet et al., 2020). The  
 165 variable used in the "denoised" wave heights, at 1 Hz (approximately 7 km)  
 166 resolution. The model tests performed and associated parameter values are  
 167 listed in table 2.4. These tests also include some wind bias correction. This  
 168 correction is defined as a piece-wise linear correction, with modeled wind  
 169 speeds above  $U_c$  multiplied by a factor  $x_c$  as follows,

$$U_{10,\text{corr}} = U_{10,\text{raw}} + x_c \max\{U_{10,\text{raw}} - U_c, 0\}. \quad (6)$$

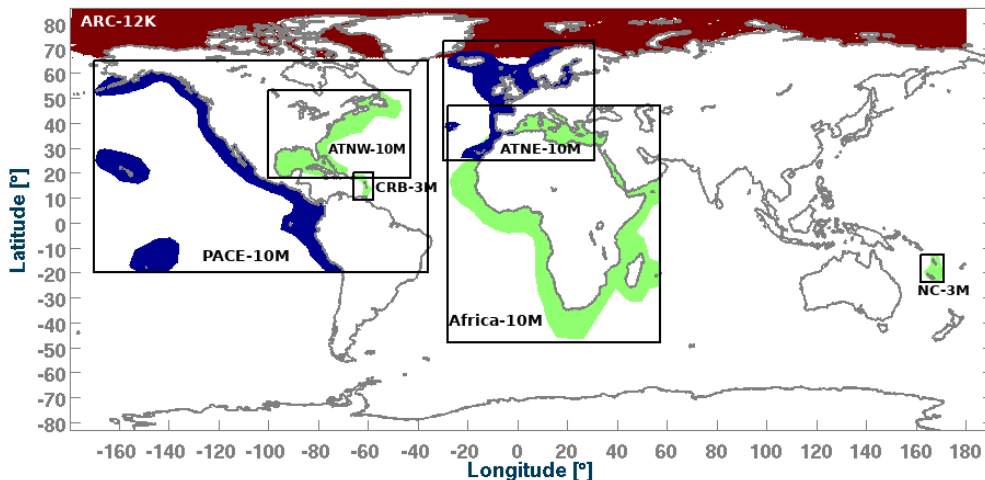


Figure 1: Sub-Grids nesting layout for multi-grid tests. Colors indicate areas where computations are performed and grids' rank in the nesting scheme: Blue is rank 2, Green is rank 3, and Red is rank 4.

170 The normalized root mean square difference (NRMSD), scatter index (SI)  
 171 and normalized mean difference (NMD) were employed to assess the model  
 172 - satellite discrepancy and its modification when model parameterizations,  
 173 forcing or discretization are modified. These statistical parameters are defined  
 174 as follows,

$$\text{NRMSD}(X) = \sqrt{\frac{\sum (X_{\text{mod}} - X_{\text{obs}})^2}{X_{\text{obs}}^2}} \quad (7)$$

$$\text{SI}(X) = \sqrt{\frac{\sum [(X_{\text{mod}} - \overline{X_{\text{mod}}}) - (X_{\text{obs}} - \overline{X_{\text{obs}}})]^2}{X_{\text{obs}}^2}} \quad (8)$$

$$\text{NMD}(X) = \frac{\sum (X_{\text{mod}} - X_{\text{obs}})}{\sum X_{\text{obs}}} \quad (9)$$

175 We note that other normalizations could be used (Mentaschi et al., 2015),  
 176 and in particular a larger scatter index is not always the indication of a worse  
 177 model, in particular in the presence of large biases or large fluctuations.

178 We particularly looked at differences for different ranges of observed val-  
 179 ues of  $H_s$ , binning all the model output as a function of the satellite values.  
 180 In general, for the model's performance assessment, attention was only paid  
 181 to  $H_s$  larger than 1.0 m because  $H_s$  smaller than 0.75 m is not very accurate

Name for set of parameters	$\beta_{\max}$	$s_7$	$Re_c$	$U_c$ (m/s)	$x_c$
T471f	1.33	$3.60 \times 10^5$	$1.50 \times 10^5$	–	–
<b>T471</b>	1.43	$3.60 \times 10^5$	$1.50 \times 10^5$	–	–
Bm1.5	1.50	$3.60 \times 10^5$	$1.50 \times 10^5$	–	–
Bm1.65	1.65	$3.60 \times 10^5$	$1.50 \times 10^5$	–	–
Bm1.7	1.70	$3.60 \times 10^5$	$1.50 \times 10^5$	–	–
Bm1.75	<b>1.75</b>	$3.60 \times 10^5$	$1.50 \times 10^5$	–	–
Bm1.65-W01	1.65	$3.60 \times 10^5$	$1.50 \times 10^5$	20	1.05
Bm1.65-W02	1.65	$3.60 \times 10^5$	$1.50 \times 10^5$	21	1.05
Bm1.65-W03	1.65	$3.60 \times 10^5$	$1.50 \times 10^5$	23	1.08
Bm1.65-W04	1.65	$3.60 \times 10^5$	$1.50 \times 10^5$	22	1.05
Bm1.7-W02	1.70	$3.60 \times 10^5$	$1.50 \times 10^5$	21	1.05
Bm1.7-W03	1.70	$3.60 \times 10^5$	$1.50 \times 10^5$	23	1.08
Bm1.7-W04	1.70	$3.60 \times 10^5$	$1.50 \times 10^5$	22	1.05
Bm1.75-W02	<b>1.75</b>	$3.60 \times 10^5$	$1.50 \times 10^5$	21	1.05
Bm1.75-W03	<b>1.75</b>	$3.60 \times 10^5$	$1.50 \times 10^5$	23	1.08
Bm1.75-W04	<b>1.75</b>	$3.60 \times 10^5$	$1.50 \times 10^5$	22	1.05
Bm1.75-W02-s7-01	<b>1.75</b>	$3.96 \times 10^5$	$1.50 \times 10^5$	21	1.05
Bm1.75-W02-s7-02	<b>1.75</b>	$4.14 \times 10^5$	$1.50 \times 10^5$	21	1.05
Bm1.75-W02-s7-03	<b>1.75</b>	<b><math>4.32 \times 10^5</math></b>	$1.50 \times 10^5$	21	1.05
Bm1.75-W02-s7-03-s4-01	<b>1.75</b>	<b><math>4.32 \times 10^5</math></b>	$1.35 \times 10^5$	21	1.05
Bm1.75-W02-s7-03-s4-02	<b>1.75</b>	<b><math>4.32 \times 10^5</math></b>	$1.20 \times 10^5$	21	1.05
<b>T475</b>	<b>1.75</b>	<b><math>4.32 \times 10^5</math></b>	<b><math>1.15 \times 10^5</math></b>	21	1.05

Table 2: Models parameters and their adjustments, in bold, leading to run T475. All parameters not specified here correspond to the default T471 parameterization (Rascle and Ardhuin, 2013; The WAVEWATCH III<sup>®</sup> Development Group, 2019). Variables  $\beta_{\max}$ ,  $s_7$   $Re_c$

,  $U_c$  and  $x_c$  correspond to namelist parameters BETAMAX, SWELLF7, SWELLF4, WCOR1 and WCOR2 in the WW3 input files (see Appendix A for the full set of parameters).

182 due to limited sampling of the signal associated with the radar bandwidth  
183 (Smith and Scharroo, 2015; Ardhuin et al., 2019).

184 Previous parameter settings defined as “T471” were used as a starting  
185 point. After gradual increases of  $\beta_{\max}$  without changing the other parameters  
186 (sets T471f to Bm1.75 as defined in table 2.4), a persistent negative NMD  
187 for  $H_s$  values larger than 7 m is found, as illustrated in Fig. 2.

188 This behavior is expected to be related to an underestimation of wind  
189 speeds in excess of 25 m/s in ECMWF IFS model results, including the  
190 ERA5 data set, as analyzed by Pineau-Guillou et al. (2018). This wind-

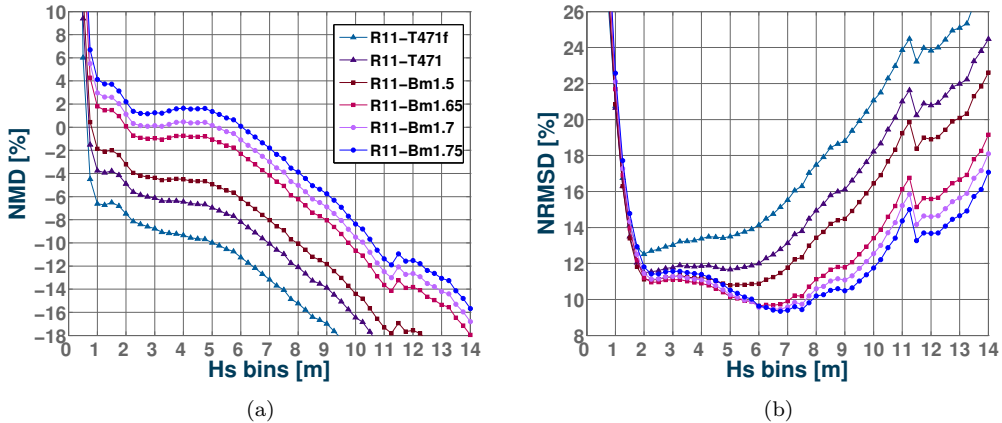


Figure 2: Error statistics for  $H_s$  for the  $\beta_{\max}$  sensitivity runs (a) Normalized mean difference between model runs – with parameters given in Table 1 – and the Jason-2 altimeter data, (b) normalized root mean square difference.

191 speed dependent bias, which is not found with CFSR winds, was the may  
 192 motivation for introducing the wind speed correction in eq. (6).

193 After setting  $\beta_{\max} = 1.75$ , wind speed corrections with the parameters  
 194 Bm1.75-W02 helped to reduce the wave heights underestimation for in the  
 195 8–14 m range (Fig. 3).

196 The wind speed  $U_c$  at which the correction kicks in is consistent with the  
 197 analysis of models and in situ wind data by Pineau-Guillou et al. (2018),  
 198 where it was demonstrated that typically strong winds above  $20 \text{ m s}^{-1}$  are  
 199 underestimated by the ECMWF models.

200 Once the NMD and NRMSD were reduced, particular attention was paid  
 201 to the distribution of  $H_s$ . The applied changes in  $\beta_{\max}$  and wind correction  
 202 lead to more intense waves in storms and swells radiated from these storms.  
 203 As a result the swell dissipation necessarily needs further tuning, which is  
 204 done here by adjusting  $s_7$  and  $Re_c$ . This adjustment can be done using wave  
 205 spectra measurements from buoys, but also using the distribution of  $H_s$ . In-  
 206 deed, the smoothing of swell dissipation was introduced in eq. (3) by Leckler  
 207 et al. (2013) to correct the sharp jump around 2 m in the distribution of  
 208 modeled  $H_s$  that was first noted by D. Vandemark (personal communication,  
 209 2012). It was only later rationalized as an effect of the Rayleigh distribution  
 210 of wave heights with turbulent boundary layers over the largest waves in a  
 211 group and viscous boundary layers over the lowest waves in a group (Perignon

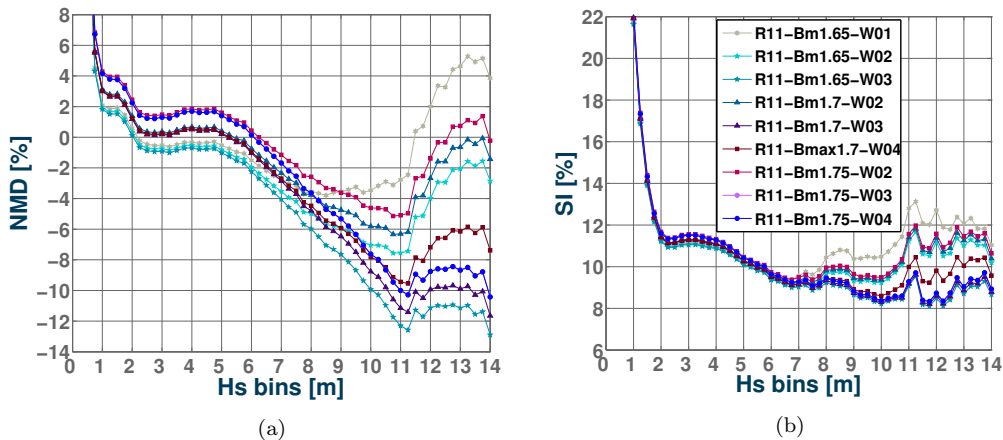


Figure 3: Error statistics for  $H_s$  for the wind correction sensitivity runs (a) Normalized mean difference between model runs – with parameters given in Table 1 – and the Jason-2 altimeter data, and (b) scatter index.

212 et al., 2014; Stopa et al., 2016b). Fig. 4 shows the distribution of  $H_s$  in the  
 213 model and observations. With panel b showing the difference between model  
 214 and observation to make the differences more visible for wave heights smaller  
 215 than 8 m, and in panel d the difference of the log of frequency of occurrence  
 216 to see the deviations for larger  $H_s$ . Augmenting  $s_7$  from  $3.6 \times 10^5$  with the  
 217 parameters S7-01 to  $4.32 \times 10^5$  with S7-03 spreads the transition from viscous  
 218 to turbulent dissipation over a wider range of  $H_s$  and tends to smooth the  
 219 histogram of  $H_s$ . This corrects the bias in the distribution around  $H_s = 2.0$  m  
 220 but makes things worse around 1.5 m. To correct those errors requires also  
 221 shifting the transition Reynolds number  $Re_c$  to lower values in runs s4-01,  
 222 s4-02 and s4-03 as shown in Fig. 5.a). These later adjustments made it  
 223 possible to match the occurrence of the highest values of  $H_s$ , up to 14 m, as  
 224 shown in Fig. 5.b).

225 Although  $H_s$  gives a very limited description of the sea state, the great  
 226 benefit of  $H_s$  altimeter data is their global coverage, and the differences  
 227 between model and observation over different regions of the world ocean can  
 228 also be revealing due to the different types of sea states found in these regions  
 229 (Chen et al., 2002), but also due to different forcing by winds, currents and  
 230 sea ice. Table 3 defines the different ocean regions for which we have looked at  
 231 regional statistics. The adjustments of  $\beta_{\max}$  and wind intensities corrections  
 232 showed particularly good improvements in the North and South Pacific. By

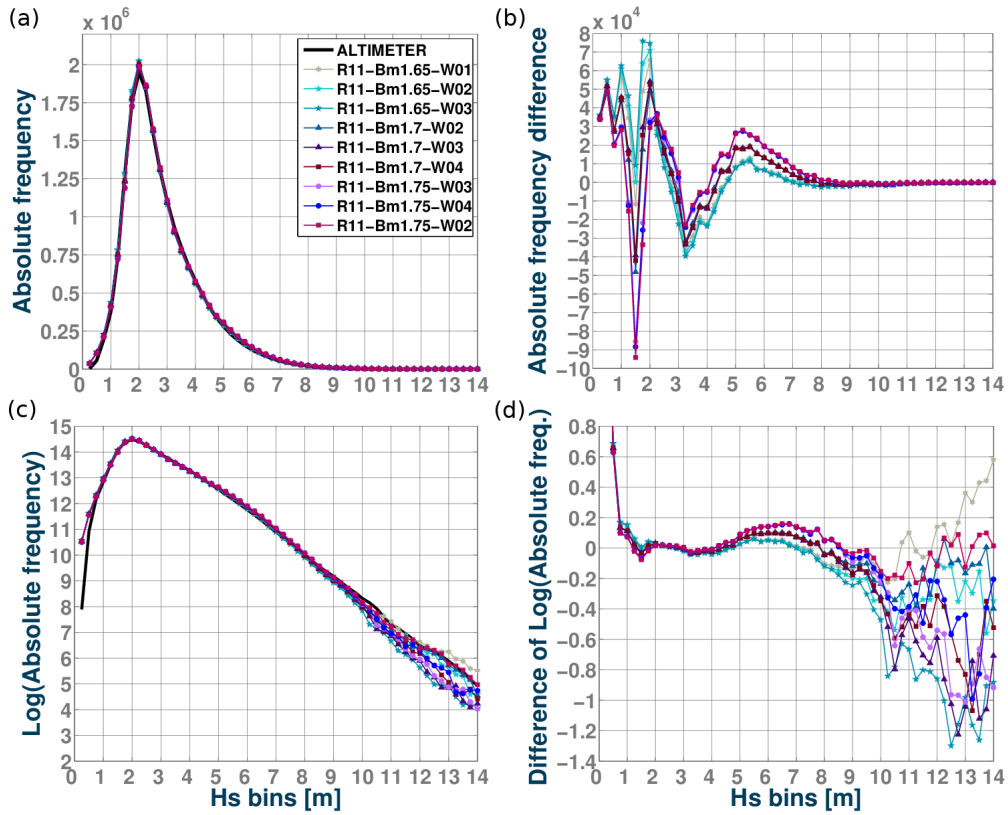


Figure 4: (a) Histogram of  $H_s$  values in the Jason – 2 and co – located model simulations. (b) Differences between the model and altimeter histograms. Plots shown are histograms.

233 only augmenting the  $\beta_{\max}$  value (for example in tests R11-Bm1.7 and R11-  
 234 Bm1.75), an important decrease of the  $H_s$  occurrences is obtained around  
 235 2 m, especially in the South Pacific, but this comes at the price of an excess  
 236 of  $H_s$  values in the 1–1.5 m range (Fig. 6).

237 Higher values of  $\beta_{\max}$  also reduced the overall negative bias in wave heights  
 238 within the range of 1.5–7 m, with a further reduction of the negative NB when  
 239 the selected wind correction is applied. This specially improves the NB for  
 240  $H_s$  of 7 to 11 m in the North Atlantic and South Pacific (Fig. 7).

241 The South Pacific stands out as a region of high positive bias (Fig. 8).

242 Although it possible that winds in the Southern Ocean may have specific  
 243 biases due to a limited set of data used for assimilation, the state of the

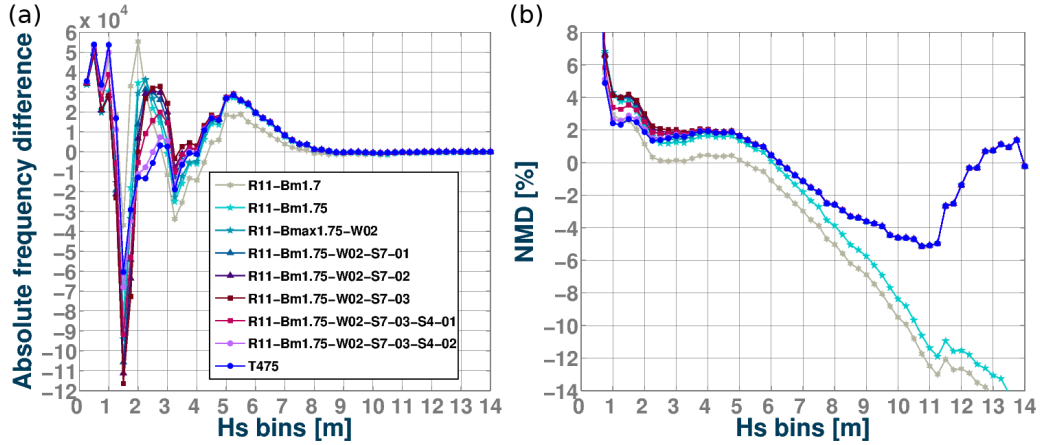


Figure 5: (a) Histogram of  $H_s$  values in the Jason-2 and model simulations absolute frequency of occurrence difference (WW3 - altimetry data) . (b) Normalized mean bias. Plots shown are from  $s_7$  and  $Re_c$  sensitivity tests.

Region (basin)	Minimum Longitude [°]	Maximum Longitude [°]	Minimum Latitude [°]	Maximum Latitude [°]
North Atlantic	-80	-5	10	50
South Atlantic	-68	20	-54	-2
North Pacific	125	-100	5	60
South Pacific	150	-73	-54	-2
Indian Ocean	50	100	-30	25
Southern Ocean	-179.98	180	-70	-55
NO SOUTH	-179.98	180	-55	66

Table 3: Regions definition for performance analysis.

244 atmosphere is very much controlled by remote sensing data, including ra-  
 245 diometers and scatterometers that are assimilated globally (Hersbach et al.,  
 246 2020).

247 Another peculiarity of the Southern Ocean is the importance of the cir-  
 248 cumpolar current that generally flows from West to East. Not taking it into  
 249 account is known to produce a large positive bias of the order of 20 cm  
 250 in wave heights due to the relative wind effect (Rascle et al., 2008; Rapizo  
 251 et al., 2018), and large gradients in  $H_s$  associated to refraction (Quilfen and  
 252 Chapron, 2019). Indeed, the relevant wind speed for wave generation is that  
 253 of the wind velocity vector relative to the surface current vector. However,

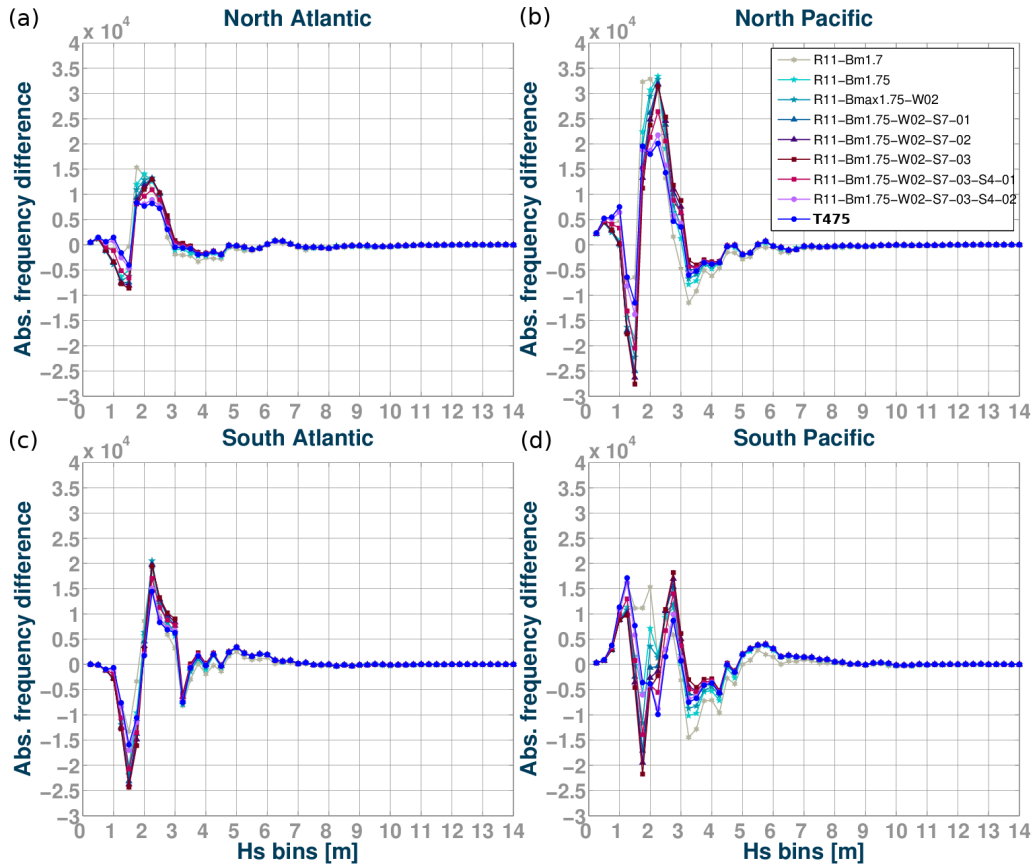


Figure 6:

254 these previous estimates use numerical models that are not very reliable for  
 255 surface current estimates (ESA, 2019). Another effect specific to the South-  
 256 ern Ocean is the presence of both sea ice and icebergs, with a very large  
 257 impact on wave heights (Ardhuin et al., 2011). The year 2011 has a rather  
 258 large anomaly in iceberg numbers, although not as large as in 2009 (Tour-  
 259 nadre et al., 2016). Finally, the details in sea ice concentration near the ice  
 260 edge and the parameterizations of wave-ice interactions are another impor-  
 261 tant source of uncertainties at latitudes south of  $55^{\circ}\text{S}$  (Doble and Bidlot,  
 262 2013; Ardhuin et al., 2020). For these reasons, we now investigate alterna-  
 263 tive forcing fields for winds, ice and currents, and their impact on the model  
 264 results.

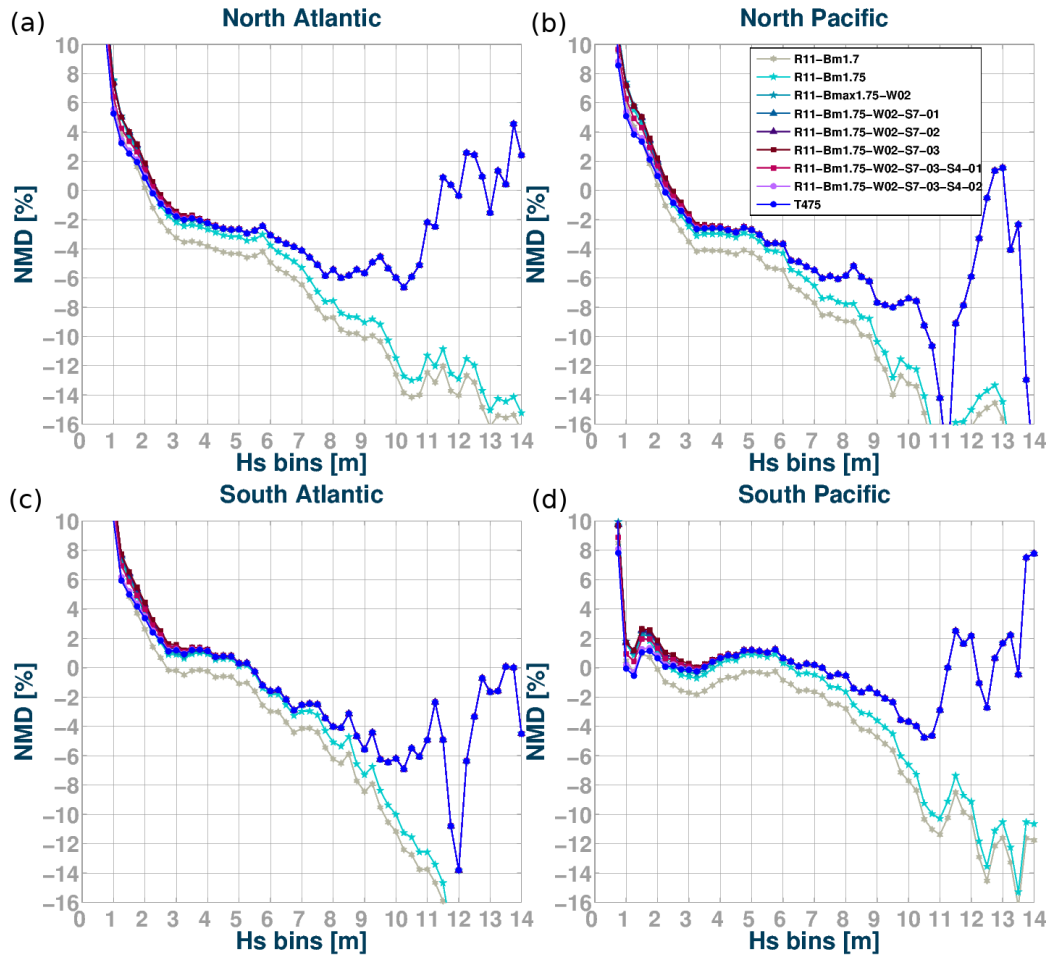


Figure 7:  $H_s$  NMD within Atlantic and Pacific basins as a function of observed wave heights.  $H_s$  bins' range is 0.25 m.

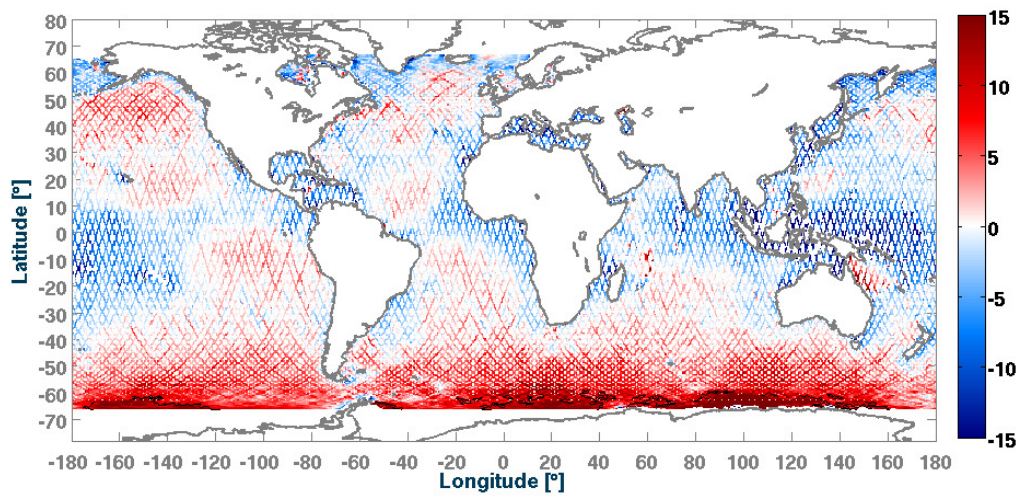


Figure 8: NMB for 1-year averaged  $H_s$  using ERA5 winds. Modelled year: 2011. Parameter settings from test T475. Colorbar indicates NMD values in %. Black lines represent positive 10 % contours.

### 265 3. Influence of forcing field choices

266 The evaluation of the model performance was done over the year 2011,  
267 with a complete validation on other years described in section 6. Whereas  
268 we had used Jason-2 data only for the model calibration, we now use the full  
269 ESA Sea State Climate Change Initiative merged altimeter data set, using  
270 the denoised 1-Hz data for the significant wave height (Dodet et al., 2020).  
271 For the year 2011 this includes data from the following satellite missions:  
272 Jason-1, Envisat, Jason-2 and Cryosat-2. Using the model with parameters  
273 T475, our baseline model run uses ERA5 winds, Ifremer sea ice and iceberg  
274 concentrations, and CMES-Globcurrent surface currents.

#### 275 3.1. Choice of forcing wind field

276 We now look at three alternative wind fields. These include the opera-  
277 tional ECMWF IFS winds which, for the year 2011, was obtained with IFS  
278 cycle 37r2, an earlier and less accurate version of IFS compared to the 41r2  
279 used for ERA5. We also considered the CFSRR winds (Saha et al., 2010)  
280 that were used by Rasclé and Ardhuin (2013). Finally we tested the Ifremer  
281 CERSAT Global Blended Mean Wind Fields (Bentamy et al., 2018), from  
282 here on just named "Ifremer".

283 The main difference between the Ifremer winds and the 2 other data sets,  
284 is that the 6-hourly surface wind fields are estimated mainly from scatterom-  
285 eter wind vector observations, merged with wind magnitude measurements  
286 from radiometer data (SSM/I, SSMIS, WindSat) and atmospheric wind re-  
287 analyzes (in particular ERA-Interim). Further details on the product and  
288 methods can be found in Bentamy et al. (2012, 2013).

289 As discussed by Rasclé and Ardhuin (2013) and Stopa et al. (2019), differ-  
290 ent wind fields are biased relative to one another. This is true for the average  
291 values around 7 m/s, and biases are even larger for high speeds over 20 m/s  
292 (Pineau-Guillou et al., 2018). This is shown again here in Fig. 9. The NCEP  
293 operational GFS model (not shown here) and CFSR hindcast both have wind  
294 speeds higher than those produced by the ECMWF models (operational IFS  
295 results and ERA5 results), leading to higher wave heights when using NCEP  
296 winds. Because the Ifremer blended wind product uses ERA-Interim as a  
297 background "filler" when observations are too far in space or time, these data  
298 sets were homogenized and the Ifremer wind has a general low bias of that  
299 corresponds to the ERA-Interim wind field.

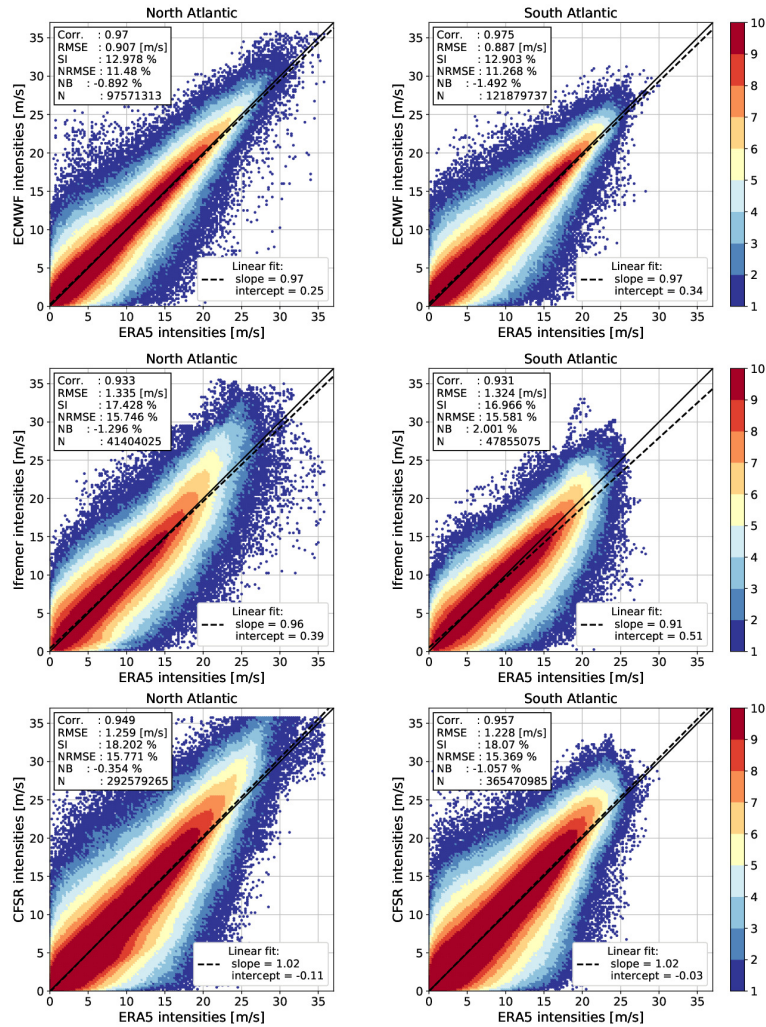


Figure 9: Scatter plot of wind speed for the months of January to July 2011. Top panels: ECMWF operational product vs ERA5, Middle panels: Ifremer vs ERA5. Bottom panels: CFSR vs ERA5. Colors give the logarithm of the number of data points in each  $0.25 \text{ m/s} \times 0.25 \text{ m/s}$  wind speed bin.

300 There is also a clear indication that ECMWF operational winds give  
 301 higher high values compared to ERA5, probably due to the higher resolution  
 302 of the operational IFS model. The consequences of these wind field properties  
 303 on the wave height biases are shown in Fig. 10.

304 Given the relative biases of the different wind datasets, it is not surprising

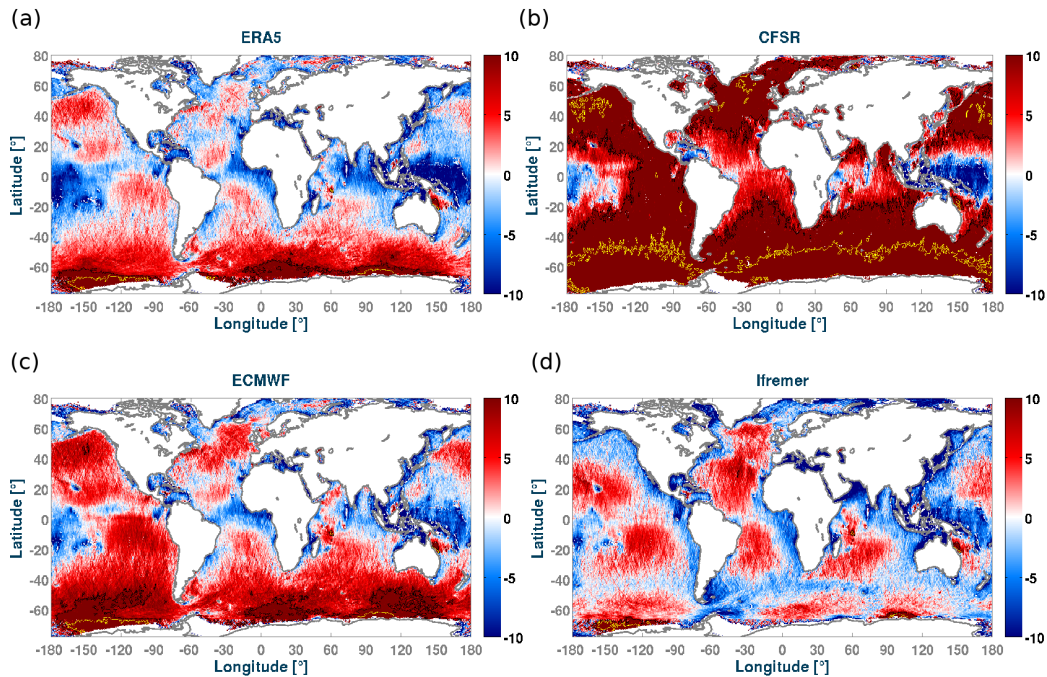


Figure 10: Normalized Mean Difference of modelled  $H_s$  minus Sea State CCI Altimeter data, averaged over the year 2011, using (a) ERA5, (b) CFSR, (c) ECMWF operational deterministic products and (d) Ifremer winds. The model was run with the set of parameters T475 as given in Table 2.4. Colorbar indicates NMD in percent. Black and yellow lines mark the +10 and +20 % contours.

305 that, without any retuning, the T475 set of parameters gives large  $H_s$  biases  
 306 when used with other wind forcing than ERA-5. In particular the CFSR  
 307 winds give positive biases larger than 15% over most of the oceans.

308 The Ifremer winds have interesting properties and are probably more  
 309 realistic in some regions, where they give lower scatter index (Fig 11.d),  
 310 including the southern ocean where the bias is also lower and significantly  
 311 different (Fig. 10.d). This difference between Ifremer and ERA5 winds is  
 312 possibly due to the fact that the remote sensing data used in the Ifremer  
 313 product generally measures a wind that is relative to the current and not an  
 314 absolute wind (Quilfen et al., 2004). There is also probably a contribution  
 315 to the generally low bias of the ERA-Iterim product that is used to fill in  
 316 between the different satellite passes.

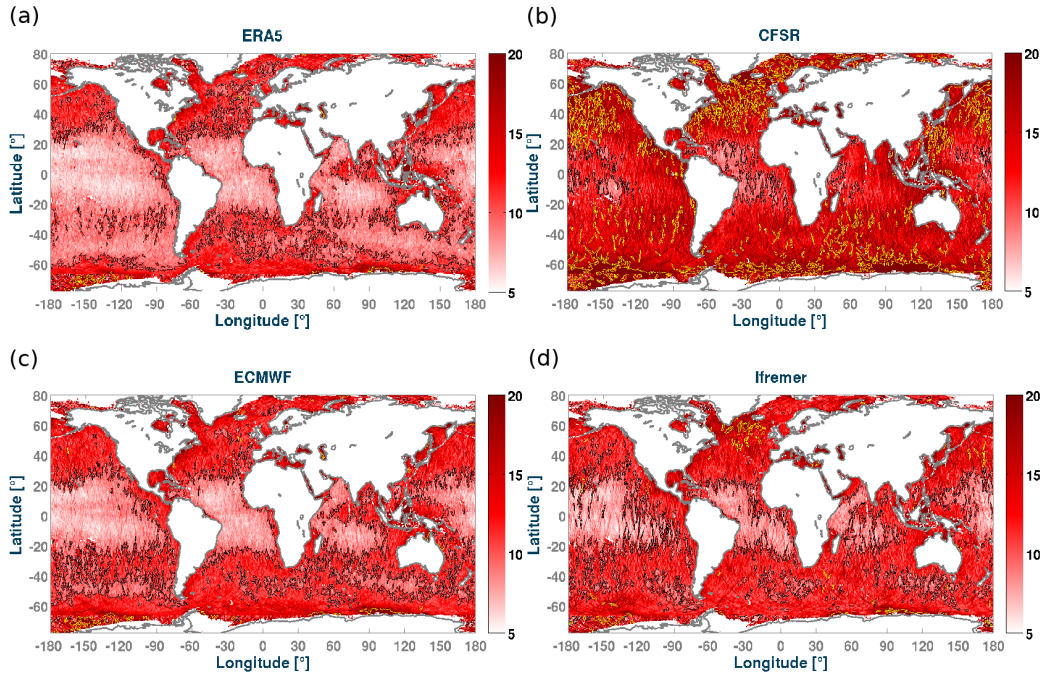


Figure 11: Scatter Index of modelled  $H_s$  minus Sea State CCI Altimeter data, averaged over the year 2011, using (a) ERA5, (b) CFSR, (c) ECMWF operational deterministic products and (d) Ifremer winds. The model was run with the set of parameters T475 as given in Table 2.4. Colorbar indicates SI in percent. Black and yellow lines mark the +10 and +20 % contours.

### 317 3.2. Effects of wave-ice parametrizations and forcing fields

318 Much work has been done on the interactions of waves and sea ice interac-  
 319 tion in the recent years, with a large emphasis on pancake ice Thomson et al.  
 320 (2018), that is particularly relevant near the ice edge and during the freeze-  
 321 up period (Doble et al., 2003). Here we have rather used a parameterization  
 322 associated to the presence of larger floes and their possible break-up induced  
 323 by waves. In particular the formulation we have used in our baseline simu-  
 324 lation was developed by Boutin et al. (2018) and adjusted by Ardhuin et al.  
 325 (2020) to 2 months of waves measured in the sea ice of the Ross sea. That pa-  
 326 rameterization combines both wave scattering in sea ice with a wave-induced  
 327 ice break-up (IS2) and dissipation below ice plates including a smooth lam-  
 328 inar to rough turbulent flow as a function of the boundary layer Reynolds  
 329 number (IC2, Stopa et al., 2016b). Given uncertainties on ice thickness,  
 330 in particular in the Southern Ocean (Williams et al., 2014) and around the

331 ice edge where it matters for wave-ice interactions, we have chosen a crude  
332 and simple constant thickness of 1 m. This parameterization is compared to  
333 the old default WW3 parameterization that is a 40 km exponential decay of  
334 wave energy proportional to the ice concentration (IC0 parameterization).  
335 The new IC2+IS2 parameterization gives a much weaker attenuation near  
336 the ice edge, and thus a larger value of  $H_s$  in the open ocean where we have  
337 data for validation (Fig. 12a,b). We have not attempted to validate the  
338 predicted wave parameter and maximum floe size in the ice-covered regions.  
339 We note that the scatter index is generally reduced around the ice, espe-  
340 cially around Greenland and in the Ross sea. These areas typically require  
341 more validation, and the model resolution ( $0.5^\circ$ ) is probably marginal for the  
342 Southern Ocean, whereas the 12 km resolution in the Arctic allows a more  
343 detailed investigation of wave-ice interactions.

344 Much less work has been devoted to the effect of icebergs, so we use  
345 here the parameterization proposed by Ardhuin et al. (2011). We verify that  
346 including icebergs has a very positive effect on reducing the bias and scatter  
347 index where the icebergs are present. For the year 2011, a large concentration  
348 of icebergs was found in both the South-East of the Pacific and the South  
349 of the Indian ocean, giving a bias reduction up to 10 percentage points and  
350 a, locally, a very large reduction in scatter index up to 6 percentage points  
351 (Fig. 12c,d). The concentration of icebergs in the South Pacific in 2011 is  
352 associated with two large icebergs, C19a and B15j, that drifted northward  
353 and eastward within the Antarctic Circumpolar Current (Tournadre et al.,  
354 2015, 2016), later breaking up into hundreds of smaller icebergs. These small  
355 icebergs are much more effective in reducing the wave energy flux, compared  
356 to a single parent iceberg, as they have a much larger cross section.

### 357 *3.3. Effect of currents*

358 Ocean surface currents can have large influences on the wave field ei-  
359 ther locally through the relative wind effect and advection, or down-wave of  
360 current gradients, due to refraction, with larger effects associated to larger  
361 current magnitude (Ardhuin et al., 2012). An important difficulty for prop-  
362 erly taking currents into account at global scales is that there are no global  
363 observations of the Total Surface Current Velocity (TSCV) that matters for  
364 wind waves, and the only proper surface measurements are made with High  
365 Frequency radar near the coasts (Barrick et al., 1974; Roarty et al., 2019). In-  
366 stead, the closest global proxy is given by the drift velocity around 15 m depth  
367 provided by instruments of the Surface Velocity Program (Elipot et al., 2016;

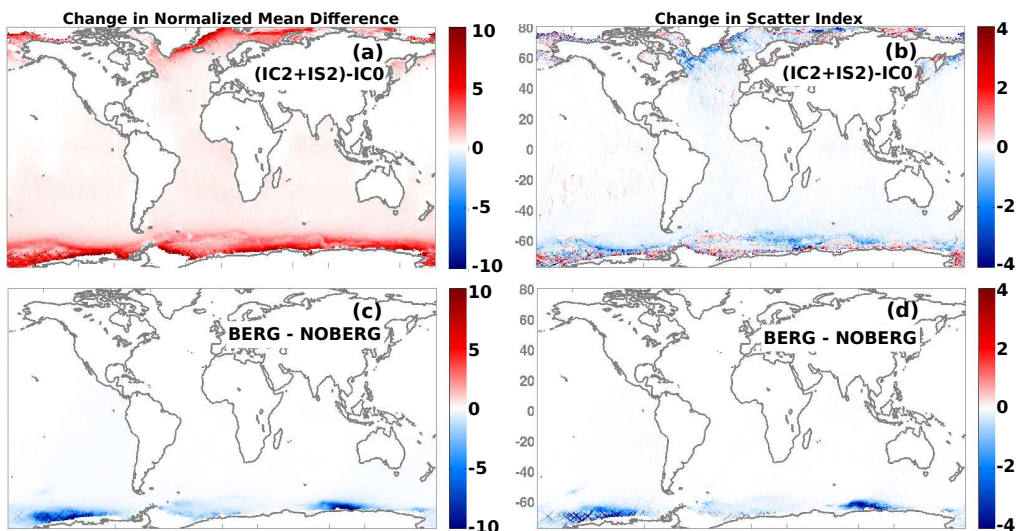


Figure 12: (a,b) using dissipation, scattering and ice break-up (IC2, IS2) or partial ice blocking (IC0) Differences in NMB and SI in percentage points for the T475 parameterization variations when using: (c,d) iceberg forcing or no iceberg forcing.

368 Lumpkin et al., 2017), with only about 1500 drifters globally giving a 500 km  
 369 resolution. We note that at the Equator and a few other places of interest,  
 370 the 15-m depth drift is often in the opposite direction of the surface drift.  
 371 Most importantly, finer spatial resolution is needed, typically down to 30 km,  
 372 to represent most of the refraction effects (Ardhuin et al., 2017a; Marechal  
 373 and Ardhuin, 2020). As a result, surface current estimates are often taken  
 374 from numerical models, or, which is the case of the CMEMS Globcurrent  
 375 product used here, derived from combined observations of sea surface height  
 376 anomaly, mean dynamic topography and surface winds, assuming a quasi-  
 377 geostrophic equilibrium of the Coriolis force associated to the surface current  
 378 with the combination of the wind stress and the pressure gradient associated  
 379 to sea surface height. Except possibly for western boundary currents such as  
 380 the Gulf Stream or the Agulhas, this approach does not work very well, in  
 381 particular around the equator and in mid-latitudes where currents are domi-  
 382 nated by near-inertial currents as illustrated in Fig. 13. The CMEMS Global  
 383 Ocean Multi Observation Products (MULTIOBS\_GLO\_PHY\_REP\_015\_004)  
 384 has an average current that is closer to the SVP drifter climatology than  
 385 the CMEMS GLORYS reanalysis, in particular around the Equator, which  
 386 is why we have chosen to use the former product as our TSCV forcing.

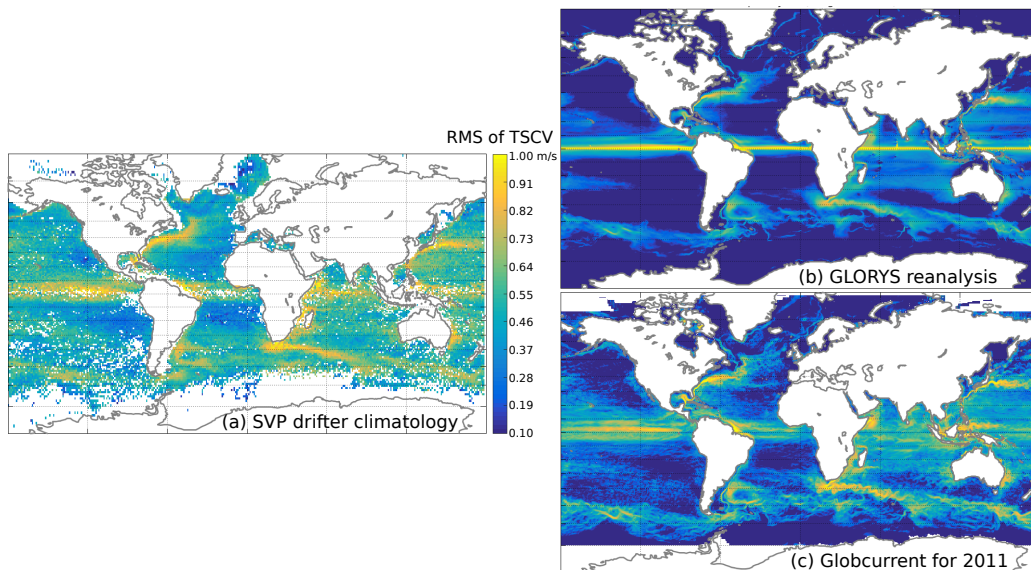


Figure 13: Root mean square current velocity (a) at 15 m depth using in situ drifter data from the Surface Velocity Program (SVP) processed by Elipot et al. (2016) with rms velocity computed over 30-day long trajectories and attributed to the center of that trajectory and white ocean pixels corresponding to 1 by 1 degree squares in which no data was available, (b) as given by the CMEMS GLORYS reanalysis, (c) as given by the CMEMS-Globcurrent product based on altimeter sea level anomalies, mean dynamic topography inferred from satellite gravimeters and ocean drifters, and "Ekman currents" estimated from ECMWF wind analyses.

387        Given all these limitations it is not too surprising that the TSCV is seldom  
 388 used at global scale.

389        Including the TSCV forcing can indeed increase errors in some regions  
 390 due to errors in the forcing field, but it generally corrects part of the bias  
 391 and gives lower scatter index for wave heights compared to altimeter data,  
 392 as illustrated in (Fig. 14). Comparing our simulation with parameters T475  
 393 with and without currents, we find a clear lower bias along the Equator and  
 394 in the Southern ocean when currents are used, as already reported by Ras-  
 395 cle et al. (2008). This is probably associated with the relative wind effect,  
 396 with wave generation given by the difference between the wind vector and  
 397 the TSCV and not the wind vector alone. We know that this approach  
 398 can overestimate the current effect when the atmosphere model is not cou-  
 399 pled with an ocean model (Hersbach and Bidlot, 2008; Renault et al., 2016),  
 400 however, we also expect that the TSCV is generally underestimated by the

401 CMEMS-Globcurrent product.

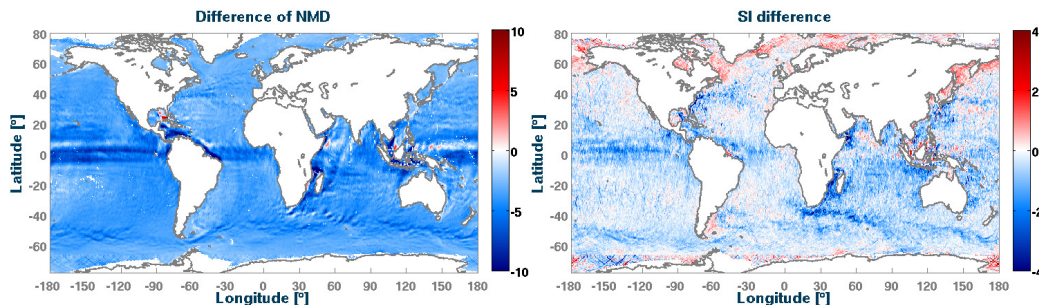


Figure 14: Left: Change in Normalized Mean Difference (NMD in percentage points) for  $H_s$  with currents and the T475 parameterization versus the same simulation without current. For both simulations the reference is the Sea State CCI  $H_s$  for the year 2011. Right: same for difference in SI, with the dark blue corresponding to a reduction of 4 percentage points (e.g. from 14% to 10%) when TSCV forcing is used.

402 The reduction of the scatter index against altimeter  $H_s$  that is brought  
403 by the current (blue regions in Fig. 14.b) clearly corresponds to the regions  
404 of strong currents where the variability of incoming waves can cause a large  
405 variability of the wave heights around the current: this is the case in the Ag-  
406 ulhas current, in the Gulf Stream, the Kuroshio, the Mozambique channel,  
407 the Somali current. However, as shown in Fig. 11, these regions are still  
408 places where the models error are relatively large, possibly due to a combi-  
409 nation of factors, including errors in the TSCV fields, insufficient directional  
410 resolution of our wave model (Marechal and Ardhuin, 2020), and insufficient  
411 spatial resolution in the TSCV field and/or the wave model. We note that  
412 the scatter index is generally increased for latitudes above  $50^\circ$  N, probably  
413 due to an insufficient resolution of the altimetry where the Rossby radius  
414 of deformation is less than 50 km (Ballarotta et al., 2019). Given the im-  
415 portance of the spectral and spatial discretizations, we now discuss these  
416 aspects.

#### 417 4. Model discretization

418 The choice of spatial and spectral discretizations can have a large impact  
419 on the model solutions, and it also has a direct and clear impact on the cost  
420 of the model, the time needed to perform the simulations. As a result, the  
421 particular choices we made for the discretizations are a compromise between

422 the computational cost and the accuracy benefits. The 28-years hindcast  
 423 used around 500,000 cpu hours distributed over 504 processors, distributed  
 424 in 18 nodes that each hold 28 CPUs and 75Gb of memory.

#### 425 4.1. Spatial resolution

426 Using higher resolution grids is critical for resolving smaller scale varia-  
 427 tions in the sea state that are caused by the time-varying forcing fields (wind,  
 428 current, sea ice) or fixed features (shoreline, water depth, bottom sediment  
 429 type and grain size). In practice, small scale gradients in wave heights are  
 430 dominated by the distance to the coast and the presence of strong currents  
 431 (Quilfen and Chapron, 2019). Because some important current system are  
 432 located close to coasts, we have chosen to define nested grids that cover the  
 433 relatively shallow waters of the coastal regions and, where possible, extend  
 434 over strong current regions (Fig. 1). As a result, our North-West Atlantic  
 435 grid covers the Grand Banks and the Gulf Stream, as well as the entire gulf  
 436 of Mexico. In a similar fashion, the Africa grid was extended to the south to  
 437 cover the Agulhas current retroflexion. Using different grids also allows to  
 tune the model parameters locally.

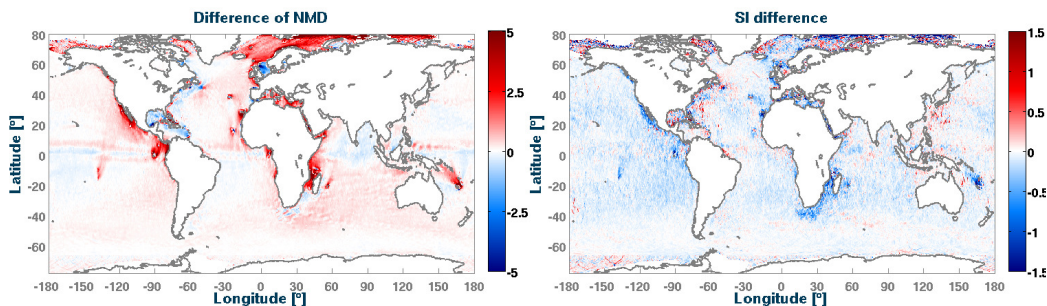


Figure 15: NMD and SI variations in percentage points for the year 2011: values for Multi-grid minus values for Single grid setup, both using the same T475 parameters. Left panel: Difference in NMD values, in this case red values represent a reduction of the negative NMD.

438 Because the wind-wave growth tuning that corresponds to T475 is very  
 439 similar to T471, it tends to give an underestimation of the wave height for  
 440 short fetches (Stopa et al., 2016a). This effect is more pronounced with higher  
 441 resolution grids, which explains the general reduction in wave height for  
 442 enclosed seas and East Coasts (stronger negative bias, in blue in Fig. 15.a).  
 443 We also find that the explicit higher resolution of shorelines and islands gives  
 444

445 larger  $H_s$  values compared to the subgrid treatment of complex shorelines and  
446 islands in a coarser grid (Chawla and Tolman, 2008), explaining the more  
447 positive bias around 140E 10S, downwave of the Tuamotus, or around the  
448 Galapagos, Azores etc. The presence of the full Arctic ocean thanks to the  
449 Arctic grid also adds wave energy that was otherwise missing in the near-  
450 global grid that stopped at 83°N.

451 Overall, the scatter index is reduced over most of the ocean with the  
452 strongest reduction in regions of strong currents like the Agulhas current, or  
453 along complex coastlines such as the Baja California peninsula (blue regions  
454 in Fig. 15.b).

#### 455 *4.2. Spectral grid and resolution*

456 However, to converge to the true solution of the wave action equation,  
457 increasing only the spatial resolution is not enough, and a finer spectral res-  
458 olution is also needed, in particular for parameters sensitive to numerical  
459 diffusion like the directional spread (Ardhuin and Herbers, 2005). Although  
460 we know that current effects on wave heights would be better resolved with 48  
461 directions instead of only 24 (Ardhuin et al., 2017b; Marechal and Ardhuin,  
462 2020), we have stuck to 24 directions only because of the much lower CPU  
463 cost, and because differences in wave heights when using 24 or 36 directions  
464 were fairly limited. Fig. 16.b shows a change in the Normalized Mean Differ-  
465 ence that is mostly limited to the tropical regions, especially around coasts  
466 and islands for which the finer directional resolution must have an impact  
467 on swell propagation, but the change in scatter index is typically much less  
468 than 1 percentage point (Fig. 16.d).

469 Compared to the costly increase of directional resolution, we found a  
470 higher benefit in terms of  $H_s$  accuracy in increasing the spectral range with  
471 a maximum frequency of 0.95 Hz instead of the 0.72 Hz used by Rascle and  
472 Ardhuin (2013). This higher frequency gives a better response, in particular  
473 for the short fetch and low wind conditions in which the peak of the wind sea  
474 would otherwise not be well resolved. In general, the values of parameters,  
475 as defined for example with T475, are tuned

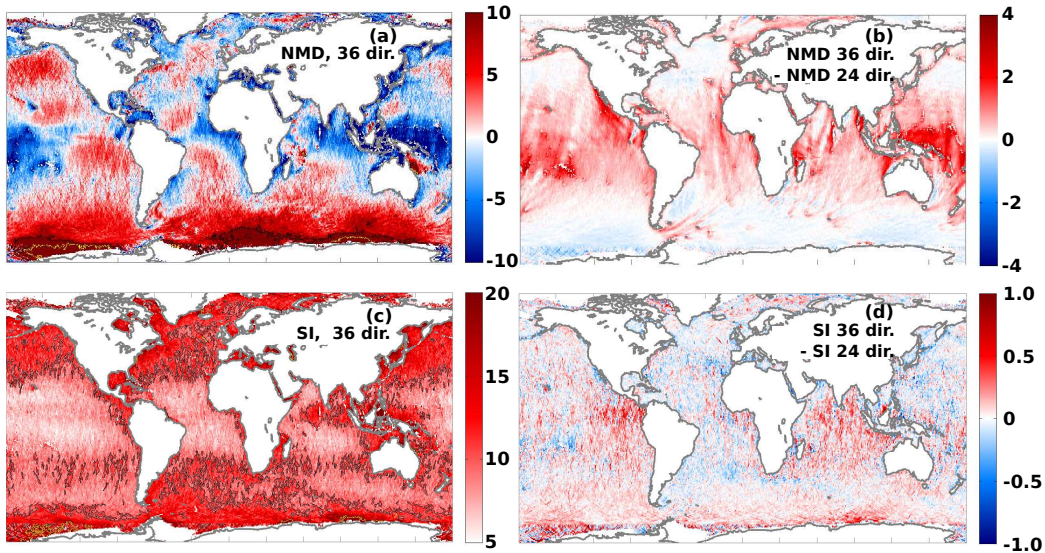


Figure 16: (a)NMD for 1 year averaged  $H_s$  using T475 with 36 directions and (b) differences in NMD for T475 with 36 directions with respect to 24 directions (Fig. 10a). Black lines mark the positive 10 % contours. (c) SI for 1 year averaged  $H_s$  using T475 with 36 directions and (d) SI difference for T475 with 36 directions with respect to 24 directions. Analyzed year: 2011. Black and yellow lines mark the positive 10 and 20 % contours respectively

476 **5. Wave directionality and alternative dissipation parameteriza-**  
 477 **tions**

478 As noted by Stopa et al. (2016b), the directional spread (Kuik et al., 1988)  
 479 is the least well predicted parameter among the most common metrics used  
 480 to define the shape of the wave spectrum. Whereas the mean direction is  
 481 well controlled by the wind evolution and the time scale of adjustment of the  
 482 wave field, the directional spread is probably influenced by details of the wave  
 483 generation and dissipation parameterizations. Here we use 3-hour averaged  
 484 data from WMO buoy 46436 in the North East Pacific as an example (see  
 485 table 4), which is the station 166 of the Coastal Data Information Program  
 486 and is maintained by Thomson et al. (2013). The correlation coefficient for  
 487  $\sigma_\theta(f)$  falls below 0.7 for frequency above 0.3 Hz. Indeed, the model has no  
 488 skill in predicting  $\sigma_\theta(f)$  for  $f > 0.5$  Hz, and the shape of the modeled spectral  
 489 tail is given by the shape at frequency  $f_m$  with an energy level decreasing like  
 490  $(f_m/f)^5$ , where  $f_m$  is a dynamically adjusted maximum prognostic frequency,  
 491 set to 2.5 times the mean frequency of the wind sea part of the spectrum.

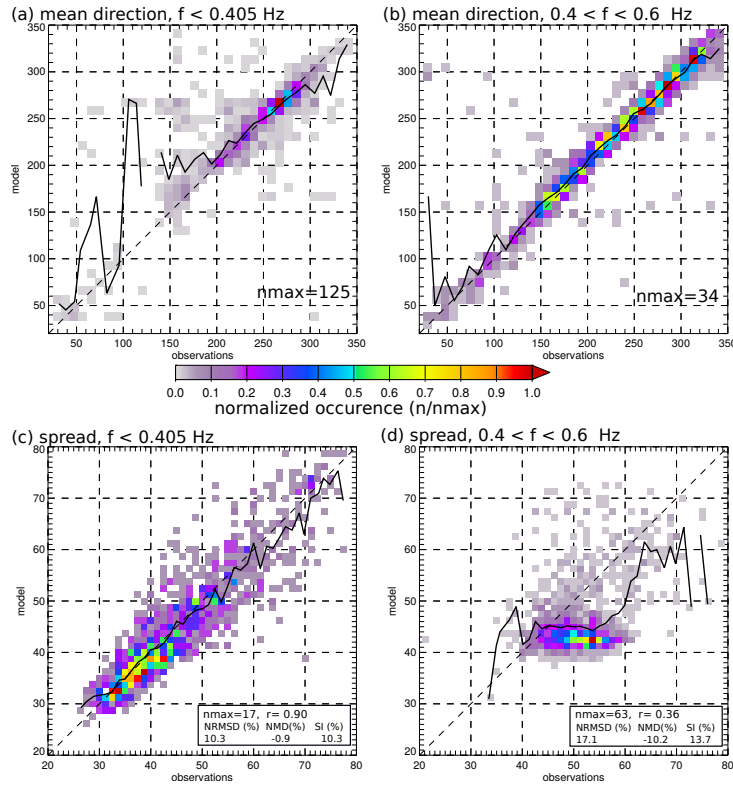


Figure 17: Modeled spread and mean direction for low frequencies ( $f < 0.4$  Hz) and high frequencies ( $f > 0.4$  Hz) at buoy 46246 for the year 2018. Colors show the number of 3 hour records for which the model-buoy pair falls in one bin, as normalized by the maximum value  $n_{max}$ . The solid lines gives the mean modeled value for each observation bin.

492 We note that the directional spread at low frequencies is, close to coasts,  
 493 very sensitive to shoreline reflections (Ardhuin and Roland, 2012). Whereas  
 494 this has a limited impact on most wave parameters, it is a critical contribution  
 495 to microseism and microbarom sources (Stutzmann et al., 2012; De Carlo  
 496 et al., 2021). In the present hindcast we have not used the slope-based  
 497 reflection coefficient proposed by Ardhuin and Roland (2012) because of the  
 498 difficulty of defining the proper slope and mixed results when validating  
 499 modeled microseisms. Instead, we have used constant reflexion coefficients of  
 500 5%, 10% and 20% for the resolved shorelines, subgrid shorelines and icebergs,  
 501 respectively. Clearly that parameterization will have to be tested and futher  
 502 improved upon using buoy directional spreads together with microseism and  
 503 microbarom data.

504 The T475 parameterization is thus still fairly poor for the frequency range  
505 0.4 to 1 Hz when the waves are developed (when the wind sea peak frequency  
506 is below 0.15 Hz), in particular for the directional distribution, which is  
507 critical for the ratio of crosswind to downwind mean square slope Munk  
508 (2009), wave breaking statistics (Romero et al., 2017) and the sources of  
509 microseisms and microbaroms at seismic or acoustic frequencies above 0.8 Hz  
510 (Farrell and Munk, 2010; Peureux and Ardhuin, 2016; De Carlo et al., 2020).  
511 Recent work have suggested that the shape of the dissipation function could  
512 be better described by Romero (2019), giving the T700 set of parameters in  
513 the WAVEWATCH III model, available in versions 7.0 and above. In T700,  
514 the ad hoc and not very effective cumulative term of Ardhuin et al. (2010) is  
515 replaced with a cumulative term that could be explained by the straining of  
516 short waves caused by long waves (Peureux et al., 2020). Preliminary tests  
517 reveal n interesting behavior for the shape of the high frequency spectrum  
518 (Fig. 18), which allows to remove the imposed diagnostic tail for  $f > f_m$   
519 thanks to a completely local (in the spectral sense) parameterization of the  
520 breaking probability, and the added cosine-squared angular dependence in  
521 the parameterization of the cumulative effect. Possibly this imposed shape  
522 of the cumulative term will have to be revised, as for example an isotropic  
523 spectrum of long waves should produce an isotropic effect unless it is a joint  
524 effect of the long and short waves. However, Romero (2019) has produced  
525 the first parameterization that is able to produce larger cross-wind slopes  
526 than down-wind slopes for wavelengths around 1 m (after 7 hours in Fig.  
527 18.d, the dominant direction for mss1 in T700NL2 is indeed the cross-wind  
528 direction), which are critical to explain the first of the inconvenient sea truths  
529 highlighted by Munk (2009).

530 Taken "out of the box" without the present retuning, the Romero (2019)  
531 parameterization performs similarly to T471 in terms of scatter index but  
532 has a 2 to 6% higher value of wave height (Fig. 19) that will also require an  
533 adjustment of the swell dissipation. The benefits of such a parameterization  
534 will probably be most important for the model parameters that are most  
535 sensitive to the high frequencies, including the mean square slope, and will  
536 require an important upgrade of the wave model in the way these shorter  
537 wave components are treated, so that the wave model result can be validated  
538 with radar back-scatter data (e.g. Noguier et al., 2016). This effort is beyond  
539 the scope of the present paper and will be discussed in Part 4.

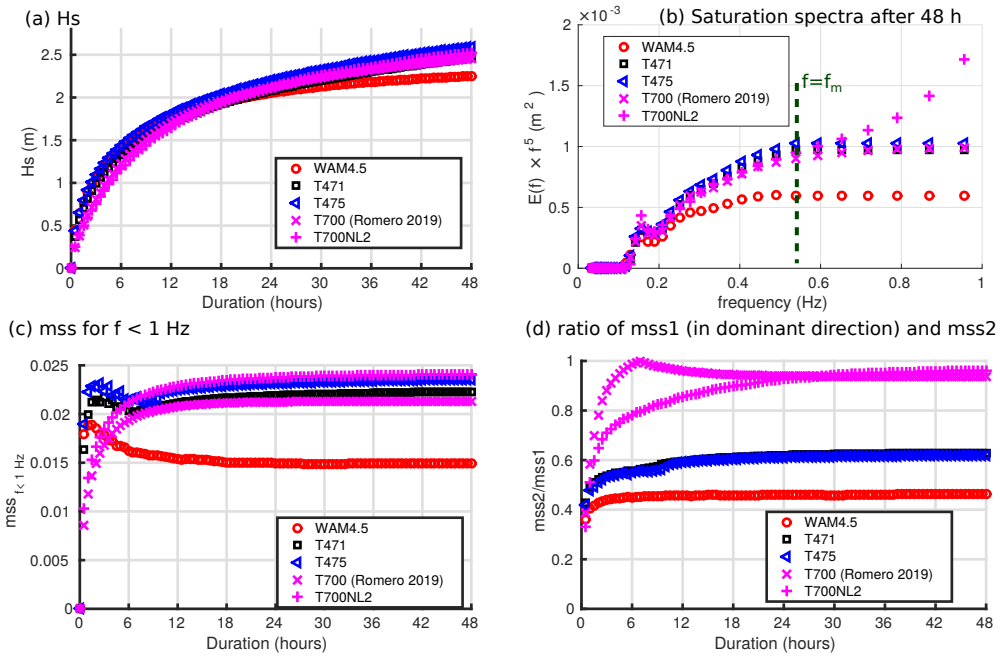


Figure 18: Differences in model results for an academic case considering a uniform ocean and a constant wind speed of 10 m/s starting from no waves. The WAM4.5 parameterization is close to the one used in the ERA5 reanalysis, and the T700NL2 corresponds to the parameterization of Romero (2019) with the non-linear interactions computed with the exact Webb-Resio-Tracy method van Vledder (2006).

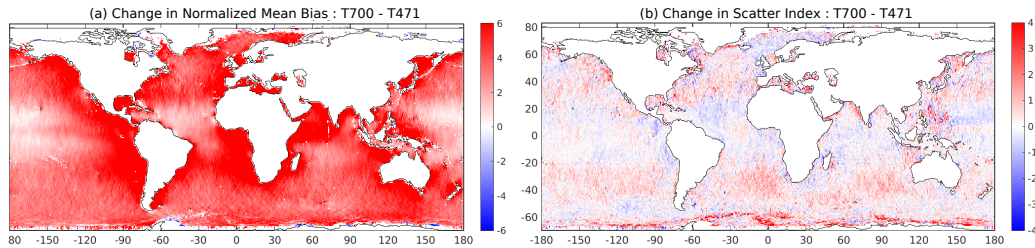


Figure 19: Change in NB and SI from the T471 to T700 change in parameterization for the year 2018. These simulations did not include ocean currents.

## 540 6. Validation

### 541 6.1. Validation with altimeter data

542 An important concern about numerical wave model hindcasts for all ap-  
 543 plications is their consistency in time which can be compromised by the

544 time-evolving error statistics of the forcing fields (winds, currents, sea ice)  
 545 and/or of the assimilated data which may both introduce time varying biases  
 546 and jumps, possibly requiring the statistical adjustment of the forcing fields  
 547 (e.g. Stopa et al., 2019) or the correction of the model results. It is thus necessary  
 548 to verify the consistency of the model output over time. This requires  
 549 validation data that are stable in time. Here we use the satellite altimeter  
 550  $H_s$  measurements of Dodet et al. (2020) that were especially designed for  
 551 this purpose, and we look at the evolution of the NMB and SI over the years  
 1997 to 2018 (Fig. 20). We find a general agreement over the years, with

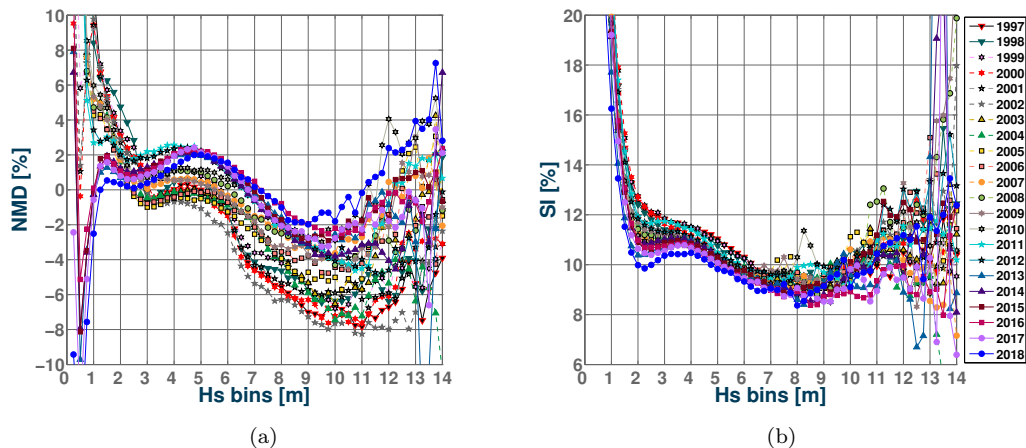


Figure 20: Performance parameters for 22 years hindcast using T475. (a)  $H_s$  NMD curves and (b) SI curves.  $H_s$  bin size is 0.25 m. Altimeters used for validation: Topex (1997-2002), Envisat (2003-2010), Jason-2 (2011-2012), Saral (2013-2018).

552 lower variations of the mean difference than was found by Rascle and Ard-  
 553 huin (2013) when using CFSR winds, and which had to be corrected in later  
 554 hindcasts (Stopa et al., 2019). Still, the changes from -1 to 2% for the bulk  
 555 of the data ( $1.5 < H_s < 4$  m) suggest a systematic drift in either the ERA5  
 556 wind speeds or the altimeter data, with relatively flatter biases as a function  
 557 of  $H_s$  for the years 2011-2018 (but still a decrease in the mean model values  
 558 or an increase in the altimeter values), and steeper  $H_s$ -dependent biases for  
 559 the years 1997-2010. The scatter index shown a general reduction of the  
 560 random differences that can be caused by a reduction in the random noise  
 561 of satellite altimeter data for the more recent missions and an improvement  
 562 in the quality of the ERA5 wind fields thanks to the assimilation of a richer  
 563 set of data (Hersbach et al., 2020).  
 564

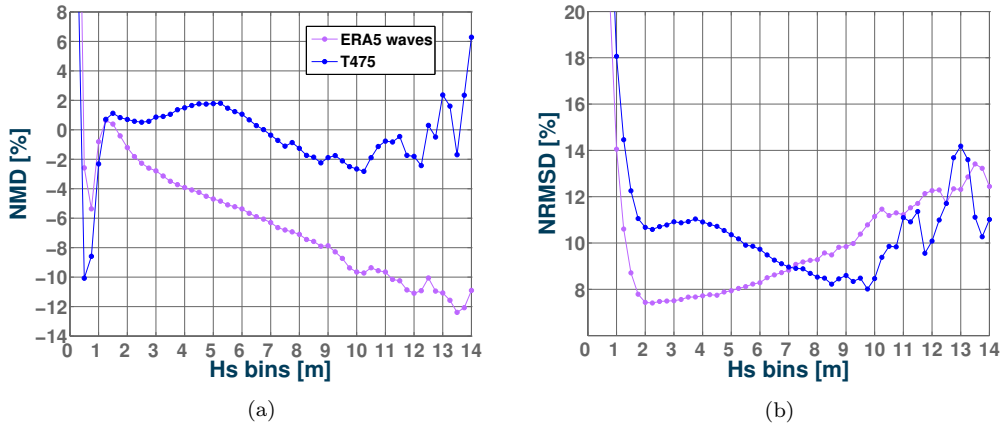


Figure 21: Performance parameters curves for test T475 and ERA5 wave product with respect to Jason-3 altimeter data. (a)  $H_s$  NMD, and (b) NRMSD. Analyzed year: 2018.  $H_s$  bin size is 0.25 m.

## 565 6.2. Comparison to ERA5 wave heights

566 Because the ERA5 reanalysis also included a wave model it is questionable  
 567 that our efforts have any added value, especially because the ERA5 wave  
 568 model assimilates altimeter wave heights and uses a wind forcing at the 10  
 569 minutes time step of the atmospheric circulation model to which it is coupled.  
 570 However, we know (J.R. Bidlot, personal communication) that the same  
 571 ECMWF wave model that uses improved wave generation and dissipation  
 572 parameterization in the IFS cycle 46R1 that is operational as of June 6, 2019  
 573 (ECMWF, 2019) and is similar to T471, already gives better results than the  
 574 ERA5 wave heights at buoy locations. It is thus interesting to look at the  
 575 differences between the ERA5 wave heights and the results of the present  
 576 hindcast. We note that our model uses different forcing, in particular for  
 577 currents, sea ice and icebergs, includes some shoreline and iceberg reflexion  
 578 and produces different output parameters, including fluxes of energy between  
 579 the ocean and atmosphere, in addition to the parameters that can be derived  
 580 from the wave spectrum. Here we only compare the two simulations, the  
 581 ERA5 which assimilated satellite altimeters, using the Jason-3 data for 2018,  
 582 which has not been assimilated in ERA5.

583 Fig. 21 shows a very strong negative bias in the ERA5 wave heights, that,  
 584 combined with a much lower random errors, gives larger rms differences for  
 585  $H_s > 7$  m. Looking at the spatial distribution of these errors we typically find

586 larger random errors in the Southern ocean with T475 compared to ERA5  
 587 wave heights, possibly a benefit of the assimilation of the other satellite  
 588 missions where the satellite tracks are most dense, and we find lower random  
 589 error in a few specific areas with T475, including in the Agulhas current,  
 590 which shows again the benefit of properly including ocean surface currents  
 in a wave model.

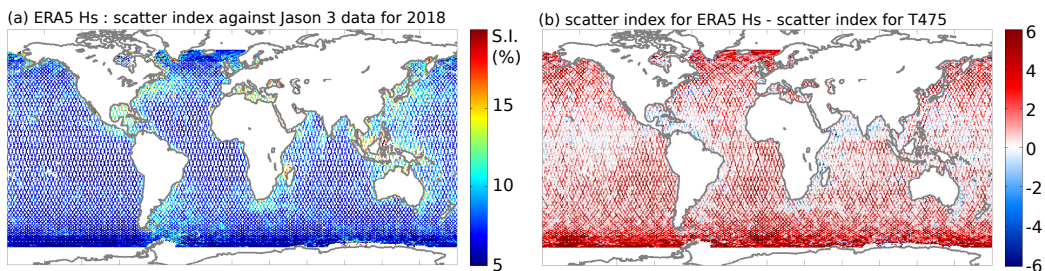


Figure 22: (a) Scatter Index for 1 year (2018) averaged ERA-5  $H_s$  with respect to Jason-3 altimeter data. (b) Difference in scatter index between T475 and ERA-5 waves product.

591

### 592 6.3. Validation with buoy data

593 So far all of our analysis, except for a brief discussion of mean direc-  
 594 tion and directional spread, has been based on wave heights alone, whereas  
 595 our model hindcast is based on the simulation of ocean wave spectra and  
 596 produces a wide range of spatially gridded parameters as well as spectra at  
 597 selected locations: around 10,000 points all along the world coastline plus the  
 598 locations of moored buoys and a few additional offshore points. Even though  
 599 the model was only marginally changed compared to the version validated  
 600 by Stopa et al. (2016a), it is interesting to look at errors on the shape of  
 601 spectra and wave period and directions parameters.

602 These comparisons are not simple because of the large response differences  
 603 of different buoy types for wavelengths shorter than 10 m ( $f \simeq 0.4$  Hz) in  
 604 particular 3-m diameter discus buoys tend to filter frequencies above 0.4 Hz  
 605 which are well reproduced, up to 0.6 Hz by 0.8 m diameter Waverider buoys  
 606 (e.g. Ardhuin et al., 2019). We thus focus on the 0.05 to 0.4 Hz frequency  
 607 band. Another difficulty is that most Waverider buoys are located in coastal  
 608 areas. We have particularly selected 5 buoys that are representative of differ-  
 609 ent wave climates, as listed in Table 4. The buoy heave spectra were averaged  
 610 over 3 h intervals.

WMO code	latitude	longitude	depth	shore distance	buoy type
46246	50.0N	145.2 W	4252 m	900 km	Datawell WR
51208	22.285 N	159.574 W	200 m	5 km	Datawell WR
51004	17.53 N	152.25 W	5183 m	300 km	3-m discus
42097	25.7 N	83.65 W	81 m	130 km	Datawell WR
44098	42.8 N	70.17 W	77 m	37 km	Datawell WR

Table 4: List of buoys selected for detailed validation over the year 2018

611 Fig. 23 shows different validations of the spectral content of the wave spectrum. The average wave spectra in Fig. 23.a reveal a general good

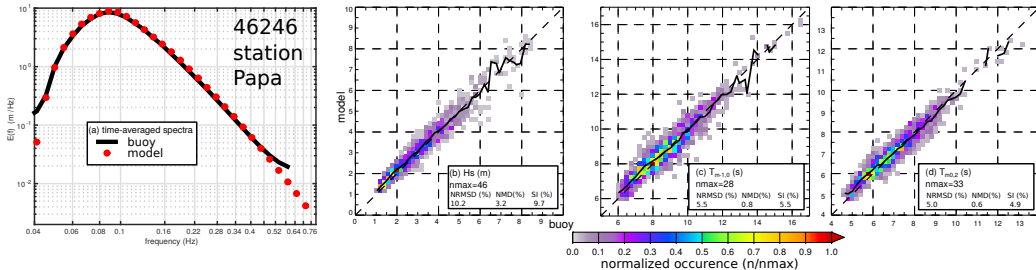


Figure 23: Modeled and measured mean spectra, scatter plots for  $H_s$ , and mean periods  $T_{m-1,0}$ ,  $T_{m0,2}$  at selected buoys 46246.

612  
613 behavior of the model compared to Datawell buoy measurements with mean  
614 differences under 10% in the frequency range 0.05 to 0.4 Hz. The deviation  
615 at low frequencies can be due to the presence of infragravity waves in the  
616 buoy measurements which were not included in our model simulation, but  
617 could have been added and have a typical height of 1 cm in the open ocean  
618 (Ardhuin et al., 2014). That deviation could also be the result of mooring  
619 line effects. At high frequencies, the model underestimation for  $f > 0.5$  Hz  
620 may be due to the buoy heave resonance (Datawell, 2014).

621 The variability of the energy content at different frequencies is generally  
622 well captured by the parameters  $H_s$  and mean periods  $T_{m0,2}$  (which is more  
623 sensitive to the high frequencies) and  $T_{m-1,0}$  (more sensitive to the low fre-  
624 quencies). With a bias under 1% and a scatter index around 5%, the model  
625 is particularly accurate for the shape of the wave spectrum.

## 626 7. Conclusions

627 The present paper discussed the influence of forcing fields (winds, sur-  
628 face current, sea ice concentration, iceberg concentration), parameterizations  
629 (wind-wave generation and swell damping) and resolution (in physical and  
630 spectral space) on the wave heights produced by a wave model hindcast, us-  
631 ing the WAVEWATCH III modelling framework and satellite-derived wave  
632 heights. It is unfortunately not practical to test all the possible combina-  
633 tions of model settings, but we expect that the choice of forcing fields and  
634 adjustment of parameters is generally robust, and the measurements shows  
635 that the present hindcast, in the context of the Integrated Ocean Waves for  
636 Geophysical and other Applications (IOWAGA) project, is generally superior  
637 to the previous version described by Rascle and Ardhuin (2013), and in some  
638 regions and for large wave heights is superior to the ERA5 reanalysis.

639 For the forcing, we found that ERA5 winds, once corrected for a low bias  
640 at wind speeds above 21 m/s, gave more accurate results than operational  
641 ECMWF analyses or the CFSR reanalysis. Alternative merged satellite-  
642 model products (Bentamy et al., 2018) gave interesting results. We also  
643 found that the use of currents provided by CMEMS-Globcurrent generally  
644 improved the model results. Probably because these current estimates are  
645 missing a significant part of the Total Surface Current Velocity, they degraded  
646 the model results at latitudes larger than 50° N. Finally, we confirmed the  
647 importance of both sea ice and icebergs for Southern Ocean and Arctic wave  
648 heights.

649 For the model parameterizations of air-sea interactions, we have shown  
650 that the distribution of  $H_s$  around the global maximum of 2 m, could be  
651 used to adjust the transition from a laminar to a turbulent boundary layers  
652 above the waves, that is very important for the attenuation of swells, and is  
653 probably the most sensitive part of the model parameterizations.

654 Regarding model discretizations, we have found a great benefit in includ-  
655 ing the 0.7 to 1 Hz frequency range, even though the directionality in that  
656 range is not yet well described by the model when waves are developed.

657 For all these tests, we have only performed limited validation for other  
658 parameters besides the significant wave height. We expect that future adjust-  
659 ments will particularly focus on the high frequencies ( $f > 0.4$  Hz) with more  
660 validation of the variables that are most sensitive to that frequency range,  
661 starting with the mean square slope and its directional components. In this  
662 respect, we expect to produce a Part 4 update on the present work based on

663 the parameterizations of Romero (2019) and a much better treatment of the  
664 model high frequencies that would make it consistent with remote sensing  
665 data, as analyzed by Noguier et al. (2016) or Yueh et al. (2006), following  
666 the work of Elfouhaily et al. (1997).

## 667 **Acknowledgments**

668 The present work was supported by ESA Climate Change Initiative Pro-  
669 gram, EU ERANET Resource code and CNES. Buoy data were furnished  
670 by the Coastal Data Information Program (CDIP), Integrative Oceanogra-  
671 phy Division, operated by the Scripps Institution of Oceanography, under  
672 the sponsorship of the U.S. Army Corps of Engineers and the California De-  
673 partment of Parks and Recreation. <https://doi.org/10.18437/C7WC72>. We  
674 are grateful to many colleagues, including Abderrahim Bentamy, Guillaume  
675 Dodet and Camille Lique for many constructive discussions.

## 676 **Appendix A. Detailed model implementation**

677 The wave model hindcast and tests presented here all use version 7.0 of  
678 WAVEWATCH III. The hindcast uses a list of switches, which appears in all  
679 NetCDF file products,

- 680 • physical parameterizations : LN1 ST4 STAB0 NL1 BT4 DB1 MLIM  
681 TR0 BS0 IC2 IS2 REF1 RWND WCOR
- 682 • advection and GSE correction: PR3 UQ
- 683 • other numerical aspects: F90 NOGRB NC4 SCRIP SCRIPNC DIST  
684 MPI FLX0 XX0 WNT2 WNX1 CRT1 CRX1 TIDE TRKNC O0 O1  
685 O2 O2a O2b O2c O3 O4 O5 O6 O7

686 The model parameters are adjusted with the same parameters for all  
687 model grids, and except for default parameter values the T475 parameters  
688 use these adjustments

- 689 • air-sea interaction parameters (SIN4 namelist) BETAMAX = 1.75,  
690 SWELLF = 0.66, TAUWSHELTER = 0.3, SWELLF3 = 0.022, SWELLF4  
691 = 115000.0, SWELLF7 = 432000.00

- 692 • wave-ice dissipation parameters (SIC2 namelist) IC2DISPER = F, IC2TURB  
693 = 1.0, IC2ROUGH = 0.001, IC2DMAX = 0.3, IC2REYNOLDS =  
694 150000, IC2SMOOTH = 200000., IC2VISC = 2.
- 695 • wave-ice scattering and floe size effects including break-up and in-  
696 elastic dissipation (SIS2 namelist): ISC1 = 0.2, IS2C2 = 0., IS2C3  
697 = 0., IS2BACKSCAT = 1., IS2BREAK = T, IS2DUPDATE = F,  
698 IS2CREEPB = 0.2E8, IS2CREEPD = 0.5, IS2CREEPN = 3.0, IS2BREAKF  
699 = 3.6, IS2WIM1 = 1.0, IS2FLEXSTR = 2.7414E+05, IS2CREEPC =  
700 0.4, IS2ANDISE = 0.55
- 701 • reflexion parameters (REF1 namelist): REF Coast = 0.05, REF-  
702 COSP\_STRAIGHT = 4, REFFREQ = 1., REFICEBERG = 0.2, REFMAP  
703 = 0., REFSLOPE=0., REFSUBGRID = 0.1, REFRMAX = 0.5
- 704 • other parameterizations (MISC namelist) ICEHINIT = 1., ICEHMIN  
705 = 0.1, CICE0 = 0.25, CICE1 = 2.00, LICE = 40000., FLAGTR = 4,  
706 FACBERG = 0.2, NOSW = 6, WCOR1 = 21., WCOR2 = 1.05 /
- 707 • activation of 3D output fields (full spectra and seismic sources, OUTS  
708 namelist) P2SF = 1, E3D = 1, I1P2SF = 3, I2P2SF = 24

## 709 **References**

- 710 Ardhuin, F., Chapron, B., Collard, F., 2009. Observation of swell dissipation  
711 across oceans. *Geophys. Res. Lett.* 36, L06607.
- 712 Ardhuin, F., Dumas, F., Bennis, A.-C., Roland, A., Sentchev, A., Forget,  
713 P., Wolf, J., Girard, F., Osuna, P., Benoit, M., 2012. Numerical wave  
714 modeling in conditions with strong currents: dissipation, refraction and  
715 relative wind. *J. Phys. Oceanogr.* 42, 2101–2120.
- 716 Ardhuin, F., Herbers, T. H. C., 2005. Numerical and physical diffusion: Can  
717 wave prediction models resolve directional spread? *J. Atmos. Ocean Technol.*  
718 22 (7), 886–895.  
719 URL <http://journals.ametsoc.org/doi/pdf/10.1175/JTECH1723.1>
- 720 Ardhuin, F., Otero, M., Merrifield, S., Grouazel, A., Terrill, E., 2020. Ice  
721 breakup controls dissipation of wind waves across southern ocean sea ice.  
722 *Geophys. Res. Lett.* 47, e2020GL087699.

- 723 Ardhuin, F., Raschle, N., Chapron, B., Gula, J., Molemaker, J., Gille, S. T.,  
724 Menemenlis, D., Rocha, C., 2017a. Small scale currents have large effects  
725 on wind wave heights. *J. Geophys. Res.* 122 (C6), 4500–4517.
- 726 Ardhuin, F., Rawat, A., Aucan, J., 2014. A numerical model for free in-  
727 fragravity waves: Definition and validation at regional and global scales.  
728 *Ocean Modelling* 77, 20–32.
- 729 Ardhuin, F., Rogers, E., Babanin, A., Filipot, J.-F., Magne, R., Roland, A.,  
730 van der Westhuysen, A., Queffelec, P., Lefevre, J.-M., Aouf, L., Collard,  
731 F., 2010. Semi-empirical dissipation source functions for wind-wave models:  
732 part I, definition, calibration and validation. *J. Phys. Oceanogr.* 40 (9),  
733 1917–1941.
- 734 Ardhuin, F., Roland, A., 2012. Coastal wave reflection, directional spreading,  
735 and seismo-acoustic noise sources. *J. Geophys. Res.* 117, C00J20.
- 736 Ardhuin, F., Stopa, J. E., Chapron, B., Collard, F., Husson, R., Jensen,  
737 R. E., Johannessen, J., Mouche, A., Passaro, M., Quartly, G. D., Swail,  
738 V., Young, I., 2019. Observing sea states. *Frontiers in Marine Sci.* 6, 124.
- 739 Ardhuin, F., Suzuki, N., McWilliams, J. C., Aiki, N., 2017b. Comments on  
740 “a combined derivation of the integrated and vertically resolved, coupled  
741 wave-current equations”. *J. Phys. Oceanogr.* 47 (9), 2377–2385.
- 742 Ardhuin, F., Tournadre, J., Queffelec, P., Girard-Ardhuin, F., 2011. Obser-  
743 vation and parameterization of small icebergs: drifting breakwaters in the  
744 southern ocean. *Ocean Modelling* 39, 405–410.
- 745 Ballarotta, M., Ubelmann, C., Pujol, M.-I., Taburet, G., Fournier, F., Leg-  
746 eais, J.-F., Faugere, Y., Delepouille, A., Chelton, D., Dibarboure, G., Picot,  
747 N., 2019. On the resolutions of ocean altimetry maps. *Ocean Science Dis-*  
748 *cussions* .
- 749 Banner, M. L., Morison, R. P., 2006. On modeling spectral dissipation due  
750 to wave breaking for ocean wind waves. In: *Proceedings of the 9th Inter-*  
751 *national workshop on wave hindcasting and forecasting*, Victoria, Canada.
- 752 Barrick, D. E., Headrick, J. M., Bogle, R. W., Crombie, D. D., 1974. Sea  
753 backscatter at HF: interpretation and utilization of the echo. *Proc. IEEE*  
754 62, 673.

- 755 Bentamy, A., Grodsky, S. A., Carton, J. A., Croizé-Fillon, D., Chapron, B.,  
756 2012. The era-interim reanalysis: configuration and performance of the  
757 data assimilation system. *J. Geophys. Res.* 117, C02011.
- 758 Bentamy, A., Grodsky, S. A., Chapron, B., Carton, J. A., 2013. Compatibility  
759 of C- and Ku-band scatterometer winds: ERS-2 and QuikSCAT. *J. Mar.*  
760 *Sys.* 117–118, 72–80.
- 761 Bentamy, A., Piollé, J. F., Prevost, C., 2018. Product user manual for wind  
762 product WIND\_GLO\_WIND\_L4\_REP\_OBSERVATIONS\_012\_006. Tech.  
763 Rep. CMEMS-WIND-PUM-012-006, EU Copernicus Marine Service.
- 764 Bidlot, J., 2005. Use of Mercator surface currents in the ECMWF forecasting  
765 system. Tech. Rep. Memorandum R60.9/JB/10104, Research Department,  
766 ECMWF, Reading, U. K.
- 767 Bidlot, J., Janssen, P., Abdalla, S., 2005. A revised formulation for ocean  
768 wave dissipation in CY25R1. Tech. Rep. Memorandum R60.9/JB/0516,  
769 Research Department, ECMWF, Reading, U. K.
- 770 Bidlot, J., Janssen, P., Abdalla, S., 2007. A revised formulation of ocean wave  
771 dissipation and its model impact. Tech. Rep. Memorandum 509, ECMWF,  
772 Reading, U. K.
- 773 Boudière, E., Maisondieu, C., Ardhuin, F., Accensi, M., Pineau-Guillou, L.,  
774 Lepesqueur, J., 2013. A suitable metocean hindcast database for the design  
775 of marine energy converters. *Int. J. Mar. Energy* 28 (3–4), e40–e52.
- 776 Boutin, G., Ardhuin, F., Dumont, D., Sévigny, C., Girard-Ardhuin, F., 2018.  
777 Floe size effects on wave-ice interactions: theoretical background, imple-  
778 mentation and applications. *J. Geophys. Res.* 123, 4779–4805.
- 779 Cavaleri, L., Bertotti, L., 1997. In search of the correct wind and wave fields  
780 in a minor basin. *Mon. Weather Rev.* 125 (8), 1964–1975.  
781 URL [http://ams.allenpress.com/archive/1520-0493/125/11/pdf/  
782 i1520-0493-125-8-1964.pdf](http://ams.allenpress.com/archive/1520-0493/125/11/pdf/i1520-0493-125-8-1964.pdf)
- 783 Chawla, A., Tolman, H. L., 2008. Obstruction grids for spectral wave models.  
784 *Ocean Modelling* 22, 12–25.

- 785 Chawla, A., Tolman, H. L., Gerald, V., Spindler, D., Spindler, T., Alves,  
786 J.-H. G. M., Cao, D., Hanson, J. L., Devaliere, E.-M., 2013. A multigrid  
787 wave forecasting model: A new paradigm in operational wave forecasting.  
788 *Weather and Forecasting* 28, 1057–1078.
- 789 Chen, G., Belcher, S. E., 2000. Effects of long waves on wind-generated waves.  
790 *J. Phys. Oceanogr.* 30, 2246–2256.  
791 URL <http://tinyurl.com/38cbjnk>
- 792 Chen, G., Chapron, B., Ezraty, R., Vandemark, D., 2002. A global view of  
793 swell and wind sea climate in the ocean by satellite altimeter and scatter-  
794 terometer. *J. Atmos. Ocean Technol.* 19, 1849–1859.
- 795 Datawell, 2014. Datawell - high frequency heave resonance. Tech. Rep. see  
796 <https://www.youtube.com/watch?v=OlrCKTnrhbQ>.  
797 URL <https://www.youtube.com/watch?v=OlrCKTnrhbQ>
- 798 De Carlo, M., Ardhuin, F., Pichon, A. L., 2020. Atmospheric infrasound  
799 radiation from ocean waves in finite depth: a unified generation theory  
800 and application to radiation patterns. *Geophys. J. Int.* 221, 569–585.
- 801 De Carlo, M., Hupe, P., Le Pichon, A., Ardhuin, F., 2021. Global microbarom  
802 patterns: a first confirmation of the theory for source and propagation.  
803 *Geophys. Res. Lett.* in press.
- 804 Dee, D. P., Uppala, S. M., Simmons, A. J., Berrisford, P., Poli, P., Kobayashi,  
805 S., Andrae, U., Balmaseda, M. A., Balsamo, G., Bauer, P., Bechtold, P.,  
806 Beljaars, A. C. M., van de Berg, L., Bidlot, J., Bormann, N., Delsol, C.,  
807 Dragani, R., Fuentes, M., Geer, A. J., Haimbergere, L., Healy, S. B., Hers-  
808 bach, H., Holm, E. V., Isaksena, L., K allberg, P., K ohler, M., Matricardi,  
809 M., McNally, A. P., Monge-Sanz, B. M., Morcrette, J.-J., Park, B.-K.,  
810 Peubey, C., de Rosnay, P., Tavolato, C., Th epaut, J.-N., Vitart, F., 2011.  
811 The era-interim reanalysis: configuration and performance of the data as-  
812 simulation system. *Quart. Journ. Roy. Meteorol. Soc.* 137, 553–597.
- 813 Doble, M. J., Bidlot, J.-R., 2013. Wave buoy measurements at the Antarctic  
814 sea ice edge compared with an enhanced ECMWF WAM: Progress towards  
815 global waves-in-ice modelling. *Ocean Modelling* 70, 166–173.
- 816 Doble, M. J., Coon, M. D., Wadhams, P., 2003. Pancake ice formation in the  
817 weddell sea. *J. Geophys. Res.* 108 (C7), 3209.

- 818 Dodet, G., Piolle, J.-F., Quilfen, Y., Abdalla, S., Accensi, M., Ardhuin, F.,  
819 Ash, E., Bidlot, J.-R., Gommenginger, C., Marechal, G., Passaro, M.,  
820 Quartly, G., Stopa, J., Timmermans, B., Young, I., Cipollini, P., Donlon,  
821 C., 2020. The sea state cci dataset v1: towards a sea state climate data  
822 record based on satellite observations. *Earth System Sci. Data* 12, 1929–  
823 1951.
- 824 ECMWF, 2019. IFS Documentation CY46R1, Part VII: ECMWF Wave  
825 Model. Tech. Rep. 333, ECMWF, Reading, UK, 103 pp.  
826 URL <https://www.ecmwf.int/node/19311>
- 827 Elfouhaily, T., Chapron, B., Katsaros, K., Vandemark, D., 1997. A unified  
828 directional spectrum for long and short wind-driven waves. *J. Geophys.*  
829 *Res.* 102 (C7), 15781–15796.
- 830 Elipot, S., Lumpkin, R., Perez, R. C., Lilly, J. M., Early, J. J., Sykulski,  
831 A. M., 2016. A global surface drifter data set at hourly resolution. *J. Geo-*  
832 *phys. Res.* 121, 2937–2966.
- 833 ESA, May 2019. Report for mission selection: SKIM. Tech. Rep.  
834 ESA-EOPSM-SKIM-RP-3550, European Space Agency, Noordwijk, The  
835 Netherlands.
- 836 Farrell, W. E., Munk, W., 2010. Booms and busts in the deep. *J. Phys.*  
837 *Oceanogr.* 40 (9), 2159–2169.
- 838 Girard-Ardhuin, F., Ezraty, R., 2012. Enhanced arctic sea ice drift estimation  
839 merging radiometer and scatterometer data. *IEEE Trans. on Geosci. and*  
840 *Remote Sensing* 50, 2639–2648.
- 841 Hanafin, J., Quilfen, Y., Ardhuin, F., Sienkiewicz, J., Queffeulou, P., Obreb-  
842 ski, M., Chapron, B., Reul, N., Collard, F., Corman, D., de Azevedo,  
843 E. B., Vandemark, D., Stutzmann, E., 2012. Phenomenal sea states and  
844 swell radiation: a comprehensive analysis of the 12-16 February 2011 North  
845 Atlantic storms. *Bull. Amer. Meteorol. Soc.* 93, 1825–1832.
- 846 Hasselmann, S., Hasselmann, K., 1985. Computation and parameterizations  
847 of the nonlinear energy transfer in a gravity-wave spectrum. part I: a new  
848 method for efficient computations of the exact nonlinear transfer. *J. Phys.*  
849 *Oceanogr.* 15, 1369–1377.

- 850 Hersbach, H., Bell, B., Berrisford, P., Hirahara, S., Horányi, A., Muñoz-  
851 Sabater, J., Nicolas, J., Peubey, C., Radu, R., Schepers, D., Simmons,  
852 A., Soci, C., Abdalla, S., Abellan, X., Balsamo, G., Bechtold, P., Biavati,  
853 G., Bidlot, J., Bonavita, M., Chiara, G. D., Dahlgren, P., Dee, D., Dia-  
854 mantakis, M., Dragani, R., Flemming, J., Forbes, R., Fuentes, M., Geer,  
855 A., Haimberger, L., Healy, S., Hogan, R. J., Hólm, E., Janisková, M.,  
856 Keeley, S., Laloyaux, P., Lopez, P., Lupu, C., Radnoti, G., de Rosnay,  
857 P., Rozum, I., Vamborg, F., Villaume, S., Thépaut, J., 2020. The ERA5  
858 global reanalysis. *Quart. Journ. Roy. Meteorol. Soc.* 146, 1999–2049.
- 859 Hersbach, H., Bidlot, J. R., 2008. The relevance of ocean surface current  
860 in the ECMWF analysis and forecast system. In: *Proceedings from the*  
861 *ECMWF Workshop on Atmosphere-Ocean Interaction*, 10-12 November  
862 2008. ASCE.  
863 URL [www.ecmwf.int/publications/library/do/references/list/](http://www.ecmwf.int/publications/library/do/references/list/28022009)  
864 [28022009](http://www.ecmwf.int/publications/library/do/references/list/28022009)
- 865 Janssen, P. A. E. M., 1991. Quasi-linear theory of wind wave generation  
866 applied to wave forecasting. *J. Phys. Oceanogr.* 21, 1631–1642, see com-  
867 ments by D. Chalikov, *J. Phys. Oceanogr.* 1993, vol. 23 pp. 1597–1600.  
868 URL [http://journals.ametsoc.org/doi/pdf/10.1175/1520-0485%](http://journals.ametsoc.org/doi/pdf/10.1175/1520-0485%281991%29021%3C1631%3AQLTOWW%3E2.0.CO%3B2)  
869 [281991%29021%3C1631%3AQLTOWW%3E2.0.CO%3B2](http://journals.ametsoc.org/doi/pdf/10.1175/1520-0485%281991%29021%3C1631%3AQLTOWW%3E2.0.CO%3B2)
- 870 Kuik, A. J., van Vledder, G. P., Holthuijsen, L. H., 1988. A method for the  
871 routine analysis of pitch-and-roll buoy wave data. *J. Phys. Oceanogr.* 18,  
872 1020–1034.  
873 URL [http://journals.ametsoc.org/doi/pdf/10.1175/1520-0485%](http://journals.ametsoc.org/doi/pdf/10.1175/1520-0485%281987%29017%3C0845%3ATROWDT%3E2.0.CO%3B2)  
874 [281987%29017%3C0845%3ATROWDT%3E2.0.CO%3B2](http://journals.ametsoc.org/doi/pdf/10.1175/1520-0485%281987%29017%3C0845%3ATROWDT%3E2.0.CO%3B2)
- 875 Leckler, F., 2013. Observation et modélisation du déferlement des vagues.  
876 Ph.D. thesis, Université Européenne de Bretagne, Ecole doctorale des Sci-  
877 ences de la Mer, Brest, France.  
878 URL <http://tinyurl.com/leckler-thesis>
- 879 Leckler, F., Ardhuin, F., Filipot, J.-F., Mironov, A., 2013. Dissipation source  
880 terms and whitecap statistics. *Ocean Modelling* 70 (9), 62–74.
- 881 Lecocq, T., Ardhuin, F., Collin, F., Camelbeek, T., 2019. On the extraction  
882 of microseismic groundmotion from analog seismograms for the validation  
883 of ocean-climate models. *Seismol. Res. Lett.* 91, 1518–1530.

- 884 Leonard, B. P., 1991. The ULTIMATE conservative difference scheme ap-  
885 plied to unsteady one-dimensional advection. *Computational Methods in*  
886 *Applied Mechanical Engineering* 88, 17–74.
- 887 Lumpkin, R., Özgökmen, T., Centurioni, L., 2017. Advances in the applica-  
888 tion of surface drifters. *Annu. Rev. Mar. Sci.* 9, 6.1–6.23.
- 889 Marechal, G., Ardhuin, F., 2020. Surface currents and significant wave height  
890 gradients: matching numerical models and high-resolution altimeter wave  
891 heights in the agulhas current region. *J. Geophys. Res.* in press.
- 892 Mentaschi, L., Besio, G., Cassola, F., Mazzino, A., 2015. Performance eval-  
893 uation of WAVEWATCH III in the mediterranean sea. *Ocean Modelling*  
894 90, 82–94.
- 895 Munk, W., 2009. An inconvenient sea truth: Spread, steepness, and skewness  
896 of surface slopes. *Annu. Rev. Mar. Sci.* 1, 377–415.
- 897 Nouguier, F., Mouche, A., Rascle, N., Chapron, B., Vandemark, D., 2016.  
898 Analysis of dual-frequency ocean backscatter measurements at Ku- and  
899 Ka-bands using near-nadir incidence GPM radar data. *IEEE Geoscience*  
900 *And Remote Sensing Letters* 31, 2023–2245.
- 901 Perignon, Y., Ardhuin, F., Cathelain, M., Robert, M., 2014. Swell dissipation  
902 by induced atmospheric shear stress. *J. Geophys. Res.* 119, 6622–6630.
- 903 Peureux, C., Ardhuin, F., 2016. Ocean bottom pressure records from the  
904 cascadia array and short surface gravity waves. *J. Geophys. Res.* 121, 2862–  
905 2873.
- 906 Peureux, C., Ardhuin, F., Guimaraes, P. V., 2020. On the unsteady steep-  
907 ening of short gravity waves near the crests of longer waves in the absence  
908 of generation or dissipation. *J. Geophys. Res.* .
- 909 Peureux, C., Benetazzo, A., Ardhuin, F., 2018. Note on the directional prop-  
910 erties of meter-scale gravity waves. *Ocean Science* 14, 41–52.
- 911 Phillips, O. M., 1985. Spectral and statistical properties of the equilibrium  
912 range in wind-generated gravity waves. *J. Fluid Mech.* 156, 505–531.

- 913 Pineau-Guillou, L., Ardhuin, F., Bouin, M.-N., Redelsperger, J.-L., Chapron,  
914 B., Bidlot, J., Quilfen, Y., 2018. Strong winds in a coupled wave-  
915 atmosphere model during a north Atlantic storm event: evaluation against  
916 observations. *Quart. Journ. Roy. Meteorol. Soc.* 144, 317–332.
- 917 Quilfen, Y., Chapron, B., 2019. Ocean surface wave-current signatures from  
918 satellite altimeter measurements. *Geophys. Res. Lett.* 216, 253–261.
- 919 Quilfen, Y., Chapron, B., Vandemark, D., 2004. The ERS scatterometer  
920 wind measurement accuracy: evidence of seasonal and regional biases. *J.*  
921 *Atmos. Ocean Technol.* 18, 1684–1697.  
922 URL [http://ams.allenpress.com/archive/1520-0426/18/10/pdf/  
923 i1520-0426-18-10-1684.pdf](http://ams.allenpress.com/archive/1520-0426/18/10/pdf/i1520-0426-18-10-1684.pdf)
- 924 Rapizo, H., Durrant, T. H., Babanin, A. V., 2018. Current-induced dissipa-  
925 tion in spectral wave models. *Ocean Dynamics* 68, 939–955.
- 926 Rascle, N., Ardhuin, F., 2013. A global wave parameter database for geo-  
927 physical applications. part 2: model validation with improved source term  
928 parameterization. *Ocean Modelling* 70, 174–188.
- 929 Rascle, N., Ardhuin, F., Queffeuilou, P., Croizé-Fillon, D., 2008. A global  
930 wave parameter database for geophysical applications. part 1: wave-  
931 current-turbulence interaction parameters for the open ocean based on  
932 traditional parameterizations. *Ocean Modelling* 25, 154–171.  
933 URL <http://hal.archives-ouvertes.fr/hal-00201380/>
- 934 Rascle, N., Chapron, B., Ardhuin, F., Soloviev, A., 2013. A note on the direct  
935 injection of turbulence by breaking waves. *Ocean Modelling* 70, 145–151.
- 936 Renault, L., Molemaker, M. J., McWilliams, J. C., Shchepetkin, A. F.,  
937 Lemarié, F., Chelton, D., Illig, S., Hall, A., 2016. Modulation of wind work  
938 by oceanic current interaction with the atmosphere. *J. Phys. Oceanogr.* 46,  
939 1685–1704.
- 940 Rio, M.-H., Mulet, S., Picot, N., 2014. Beyond GOCE for the ocean circu-  
941 lation estimate: Synergetic use of altimetry, gravimetry, and in situ data  
942 provides new insight into geostrophic and Ekman currents. *Geophys. Res.*  
943 *Lett.* 41, 8918–8925.

- 944 Rivas, M. B., Stoffelen, A., 2019. Characterizing ERA-Interim and ERA5  
945 surface wind biases using ASCAT. *Ocean Sci.* 15, 831–852.
- 946 Roarty, H., Cook, T., Hazard, L., George, D., Harlan, J., Cosoli, S., Wyatt,  
947 L., Fanjul, E. A., Terrill, E., Otero, M., Largier, J., Glenn, S., Ebuchi, N.,  
948 Whitehouse, B., Bartlett, K., Mader, J., Rubio, A., Corgnati, L., Man-  
949 tovani, C., Griffa, A., Reyes, E., Lorente, P., Flores-Vidal, X., Saavedra-  
950 Matta, K. J., Rogowski, P., Prukpitikul, S., Lee, S.-H., Lai, J.-W., Guerin,  
951 C.-A., Sanchez, J., Hansen, B., Grilli, S., 2019. The global high frequency  
952 radar network 6, 164:1–164:23.
- 953 Roland, A., Ardhuin, F., 2014. On the developments of spectral wave models:  
954 numerics and parameterizations for the coastal ocean. *Ocean Dynamics*  
955 64 (6), 833–846.
- 956 Romero, L., 2019. Distribution of surface wave breaking fronts. *Geophys.*  
957 *Res. Lett.* 46, 10463–10474.
- 958 Romero, L., Lenain, L., Melville, W. K., 2017. Observations of surface wave–  
959 current interaction. *J. Phys. Oceanogr.* 47, 615–632.
- 960 Saha, S., Moorthi, S., Pan, H.-L., Wu, X., Wang, J., Nadiga, S., Tripp, P.,  
961 Kistler, R., Woollen, J., Behringer, D., Liu, H., Stokes, D., Grumbine, R.,  
962 Gayno, G., Wang, J., Hou, Y.-T., ya Chuang, H., Juang, H.-M. H. a. J. S.,  
963 Iredell, M., Treadon, R., Kleist, D., Delst, P. V., Keyser, D., Derber, J.,  
964 Ek, M., Meng, J., Wei, H., Yang, R., Lord, S., van den Dool, H., Kumar,  
965 A., Wang, W., Long, C., Chelliah, M., Xue, Y., Huang, B., Schemm, J.-K.,  
966 Ebisuzaki, W., Lin, R., Xie, P., Chen, M., Zhou, S., Higgins, W., Zou, C.-  
967 Z., Liu, Q., Chen, Y., Han, Y., Cucurull, L., Reynolds, R. W., Rutledge,  
968 G., Goldberg, M., 2010. The NCEP Climate Forecast System Reanalysis.  
969 *Bull. Amer. Meterol. Soc.* 91, 1015–1057.
- 970 Smith, W. H. F., Scharroo, R., 2015. Waveform aliasing in satellite radar  
971 altimetry. *IEEE TGRS* 53, 1671–1682.
- 972 Stopa, J. E., Ardhuin, F., Bababin, A., Zieger, S., 2016a. Comparison and  
973 validation of physical wave parameterizations in spectral wave models.  
974 *Ocean Modelling* 103, 2–17.
- 975 Stopa, J. E., Ardhuin, F., Girard-Ardhuin, F., 2016b. Wave climate in the  
976 Arctic 1992-2014: seasonality and trends. *The Cryosphere* 10, 1605–1629.

- 977 Stopa, J. E., Ardhuin, F., Stutzmann, E., Lecocq, T., 2019. Sea state trends  
978 and variability: consistency between models, altimeters, buoys, and seismic  
979 data (1979-2016). *J. Geophys. Res.* 124, in press.
- 980 Stutzmann, E., Schimmel, M., Ardhuin, F., 2012. Modeling long-term seismic  
981 noise in various environments. *Geophys. J. Int.* 191, 707–722.
- 982 The WAVEWATCH III<sup>®</sup> Development Group, 2019. User manual and sys-  
983 tem documentation of WAVEWATCH III<sup>®</sup> version 6.07. Tech. Note 333,  
984 NOAA/NWS/NCEP/MMAB, College Park, MD, USA, 465 pp. + Appen-  
985 dices.
- 986 Thomson, J., Ackley, S., Girard-Ardhuin, F., Ardhuin, F., Babanin, A.,  
987 Boutin, G., Brozena, J., Cheng, S., Collins, C., Doble, M., Fairall, C.,  
988 Guest, P., Gebhardt, C., Gemmrich, J., Graber, H. C., Holt, B., Lehner,  
989 S., Lund, B., Meylan, M. H., Maksym, T., Montiel, F., Perrie, W., Persson,  
990 O., Rainville, L., Rogers, W. E., Shen, H., Shen, H., Squire, V., Stammer-  
991 john, S., Stopa, J., Smith, M. M., Sutherland, P., Wadhams, P., 2018.  
992 Overview of the arctic sea state and boundary layer physics program. *J.*  
993 *Geophys. Res.* 123.
- 994 Thomson, J., D’Asaro, E. A., Cronin, M. F., Rogers, W. E., Harcourt, R. R.,  
995 Shcherbina, A., 2013. Waves and the equilibrium range at ocean weather  
996 station P. *J. Geophys. Res.* 118, 595–5962.
- 997 Tolman, H. L., 1995. On the selection of propagation schemes for a spectral  
998 wind wave model. Office Note 411, NWS/NCEP, 30 pp + figures.
- 999 Tolman, H. L., 2002. Alleviating the garden sprinkler effect in wind wave  
1000 models. *Ocean Modelling* 4, 269–289.
- 1001 Tolman, H. L., 2008. A mosaic approach to wind wave modeling. *Ocean*  
1002 *Modelling* 25, 35–47.
- 1003 Tournadre, J., Bouhier, N., Girard-Ardhuin, F., Rémy, F., 2016. Antarctic  
1004 iceberg distributions 2002–2010. *J. Geophys. Res.* 121, 327–349.
- 1005 Tournadre, J., Poisson, J. C., Steunou, N., Picard, B., 2015. Validation of  
1006 AltiKa matching pursuit rain flag. *Marine Geodesy* 38, 107–1023.

- 1007 van Vledder, G. P., 2006. The WRT method for the computation of non-linear  
1008 four-wave interactions in discrete spectral wave models. *Coastal Eng.* 53,  
1009 223–242.
- 1010 WAMDI Group, 1988. The WAM model - a third generation ocean wave  
1011 prediction model. *J. Phys. Oceanogr.* 18, 1775–1810.  
1012 URL [http://journals.ametsoc.org/doi/pdf/10.1175/1520-0485%](http://journals.ametsoc.org/doi/pdf/10.1175/1520-0485%281988%29018%3C1775%3ATWMTG0%3E2.0.CO%3B2)  
1013 [281988%29018%3C1775%3ATWMTG0%3E2.0.CO%3B2](http://journals.ametsoc.org/doi/pdf/10.1175/1520-0485%281988%29018%3C1775%3ATWMTG0%3E2.0.CO%3B2)
- 1014 Williams, G., Maksym, T., Wilkinson, J., Kunz, C., Murphy, C., Kimball,  
1015 P., Singh, H., 2014. Thick and deformed antarctic sea ice mapped with  
1016 autonomous underwater vehicles. *Nature Geosci.* 8, 61–67.
- 1017 Young, I. R., van Vledder, G. P., 1993. A review of the central role of non-  
1018 linear interactions in wind-wave evolution. *Phil. Trans. Roy. Soc. London*  
1019 *A* 342, 505–524.
- 1020 Yueh, S. H., Wilson, W. J., Dinardo, S. J., Hsiao, S. V., 2006. Polarimet-  
1021 ric microwave wind radiometer model function and retrieval testing for  
1022 windsat. *IEEE Trans. on Geosci. and Remote Sensing* 44 (3), 584–595.